ISRAPS
Bulletin

ONE-DAY DISCUSSION MEETING:

**"SPECTROSCOPY ACROSS ENERGY DOMAINS:
FROM FUNDAMENTAL TO APPLICATIONS"**

ISRAPS

Guest Editor
Dr. Beena G. Singh

A Publication of
**Indian Society for
Radiation and Photochemical Sciences**

Message from the President and Secretary, ISRAPS

Dear ISRAPS members,

Warm greetings from the Executive Council of ISRAPS!

ISRAPS has been actively engaged in organizing conferences and discussion meetings related to the frontier areas of Radiation & Photochemistry. In this regard, we take this opportunity to acknowledge all the ISRAPS Life Members and other researchers who have contributed in organizing various activities including discussion meetings of ISRAPS at different institutes across the country.

ISRAPS remains committed in promoting the advances in the research area in radiation chemistry, photochemistry and its interdisciplinary applications, including spectroscopy, nanomaterials, atmospheric chemistry, supramolecular chemistry, radiation polymerization, radiation biology, medicine, and more. Continuing our mandate of advancing academic discourse, ISRAPS recently organized the Discussion Meeting-Cum-One Day Symposium on *"Spectroscopy Across Energy Domains: From Fundamentals to Applications"* on September 28, 2024, at the Department of Chemistry, IIT Hyderabad. The event featured esteemed experts from leading research groups who delivered insightful talks on the role of spectroscopy in studying fundamental processes like molecular dynamics and its applications in energy and medicine. We express our sincere thanks to all participants and extend special gratitude to Prof. Krishna Gavvala for his pivotal role in ensuring the success of this meeting.

We thank Dr. Beena G. Singh, Guest Editor, for her effort in preparing this bulletin and all the contributing authors for making it an informative and engaging publication.

We encourage all members to actively participate in ISRAPS activities and help expand our reach by enrolling more members from their institutions. Your suggestions are always welcome, and we look forward to your involvement in our upcoming initiatives.

Dr. A.C. Bhasikuttan
President, ISRAPS

Dr. P. Mathi
Secretary, ISRAPS

Editor's Desk...

Spectroscopy is a scientific field that focuses on understanding the interaction of matter with electromagnetic radiation (EMR). The energy of EMR ranges from low-frequency radio waves to high-energy gamma rays, and the interaction of matter with EMR across this energy domain reveal key insights into molecular dynamics and structural properties. Understanding the molecular dynamics is essential for developing materials that have wide-ranging applications in fields such as materials science, medicine, and environmental monitoring.

In an effort to promote radiation and photochemical sciences, Indian Society of Radiation and Photochemical Sciences (ISRAPS) conducted a one-day discussion meeting titled *"Spectroscopy Across Energy Domains: From Fundamental to Applications"* at the Indian Institute of Technology Hyderabad, in collaboration with the Department of Chemistry, IIT Hyderabad. Continuing ISRAPS's rich tradition of publishing bulletins based on talks delivered by esteemed researchers, we are delighted to present this issue, which focuses on the application of spectroscopy across various scientific domains. This bulletin features six articles that explore the role of spectroscopy in studying fundamental processes such as molecular dynamics and in developing materials for applications in energy and medicine. The first article by Dr. Mallia highlights his work on utilization of ionizing radiation along with functionalized gold nanoparticles for developing theranostic material. Dr. Juby discusses her work on utilizing gamma radiation to develop customized polymers for sensors and drug delivery systems. Dr. Rajib article discusses the excited state dynamics of singlet fission in the polyaromatic compounds and their development as energy-efficient materials. Dr. Krishna highlights the use of photochemical methods for the qualitative analysis of Imiquimod (IMQ) in commercial creams, emphasizing their potential in pharmaceutical quality control and counterfeit detection. Additionally, Dr. Surajit introduces a novel method developed by his group for probing energy barriers in reactions involving biomolecules and their solvent complexes using two-color resonant two-photon ionization. The article by Dr. Vandana discusses her research on effect pulse duration on CH_3I dissociation, showing that shorter pulses favor low-energy fragmentation, while longer pulses lead to Coulomb explosion and complex multi-ion pathways.

Together, these articles highlight the importance of spectroscopy in investigating fundamental molecular processes and enabling the development of advanced materials for a range of applications. On behalf of ISRAPS, I sincerely thank all contributing authors for their valuable inputs to this issue.

Dr. Beena G. Singh, *Scientific Officer/G in the Radiation and Photochemistry Division, BARC. Her main area of interest is investigating the reaction mechanism of radiation induced redox reactions of organic molecules. She has published 91 articles in peer reviewed scientific journals. She is the recipient of Carl Storm International Diversity Award from the organizers of Gordon Research Conference in Radiation Chemistry, 2012 and Scientific & Technical Excellence Award from Department of Atomic Energy, 2015.*

INDIAN SOCIETY FOR RADIATION AND PHOTOCHEMICAL SCIENCES (ISRAPS)

EXECUTIVE COUNCIL (2024-2026)

Contents

Radiolabeled gold nanoparticles for possible application in therapy of hypoxic tumours

Madhava B. Mallia[a,b*]**, Sweety Mittal**[a]**, Rohit** *Sharma*[a]

[a]Radiopharmaceuticals Division
Bhabha Atomic Research Center, Mumbai - 400085, India
[b]Homi Bhabha National Institute, Anushaktinagar, Mumbai - 400094, India
Email: mallia@barc.gov.in

Abstract

Considering the role of hypoxia in cancer progression and poor prognosis, hypoxia centric theranostic approaches have immense potential in clinical cancer management. Currently, hypoxia imaging radiopharmaceuticals are used to map hypoxia in tumor followed by image guided hypoxia directed radiation therapy. Herein, a hypoxia selective theranostic nanoplatform, which can be used to deliver therapeutic dose of radiation to the hypoxic tumor tissue through systemic administration is described. In addition to delivering radiation dose to the hypoxic tumor tissue, the versatile nanoplatform developed can also be used to load radiosensitizers or chemotherapeutic drugs to enhance therapeutic effect.

Introduction

Hypoxia in tumor has a negative influence in clinical management of cancer. Primary reason for this could be attributed to the resistance of hypoxic tumor cells to radiation therapy as well as chemotherapy. Therefore, detection and quantification of hypoxia in can significantly improve the clinical management of cancer through hypoxia directly treatment strategies. Invasive methods of detecting hypoxia in tumor have inherent difficulties due to the heterogeneous nature of hypoxia. Polarographic electrode is one such probe used for direct measurement of tissue oxygen concentration and has long been applied for quantitative estimation of oxygen tension (pO_2) in various types of cancers lesions in vivo [1]. The technique requires insertion of probe inside tumor followed by measurement of current at the electrode surface due to reduction of oxygen, which is proportional to the pO2. Though this method is considered as gold standard, it is limited to accessible tumors and the invasive procedure may result in damage to the tumor tissue with possible change in the local oxygenation status [2]. In this context, non-invasive techniques provide better options for obtaining information on hypoxic status of the tumor, which could be used for planning hypoxia directed therapeutic clinical strategies. Optical imaging [3], magnetic resonance imaging (MRI) [4], and imaging using radiopharmaceuticals constitute the primary non-invasive ways for mapping hypoxia in tumor [5]. Among the imaging-based modalities for hypoxia assessment, use of radiopharmaceuticals is currently the preferred choice in clinical settings and has been extensively used for planning hypoxia directed therapy [6].

Radiopharmaceuticals

Radiopharmaceuticals are radioisotope tagged molecules that can be safely administered, either orally or intravenously, in human body for the purpose of carrying out organ function evaluation, diagnosis or treatment of a variety of patho-physiological conditions including cancer. A very distinctive feature of radiopharmaceuticals from pharmaceuticals that we use in our day-to-day life is its use in very low concentrations (10^{-6} M - 10^{-9} M) insufficient to elicit any pharmacological effects. A general radiopharmaceutical design consists of a molecule that can accumulate in a
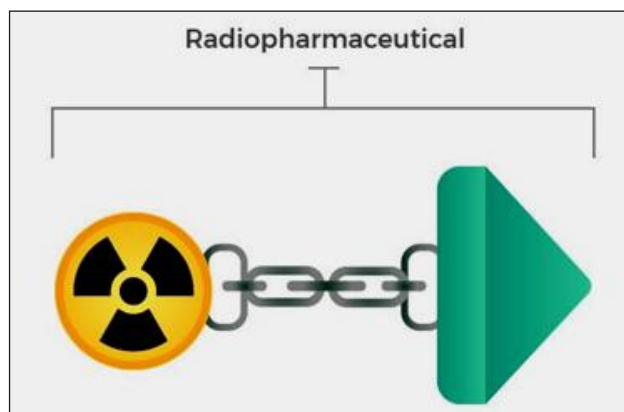
Figure 1. *Typical design of a radiopharmaceutical*

specific organ/tissue or trace the path of various physiological processes inside the body to which a radionuclide is chemically attached through a linker [Figure 1]. The selection of the radionuclide used in the radiopharmaceutical depends on the purpose for which the radiopharmaceutical is designed. Radioisotopes which emit gamma radiation or positrons are used in diagnostic radiopharmaceuticals. The highly penetrating gamma radiations emanating coming out of the patients body forms the signal for the detectors in gamma camera to produce images (also called scans) that show the distribution of radiopharmaceutical inside the patient. The positrons generate gamma photons indirectly. Positrons interact with the electron present in the surrounding medium and an annihilation reaction occurs. The annihilation reaction results in two 511 keV gamma rays emitted in opposite directions which are detected simultaneously to construct the image. Single photon emission tomography (SPECT) and positron emission tomography (PET) are the two imaging modalities used in nuclear medicine depending on the type of emission by the radionuclide. When tagged with an alpha or beta-emitting radioisotope we obtain a therapeutic radiopharmaceutical. Therapeutic radiopharmaceuticals deliver therapeutic dose of radiation to the tumor site. The high-LET (linear energy transfer) radiations from the therapeutic radioisotope cause damage to the cancer cells by direct or indirect effect, resulting eventually resulting in the death of the cancer cell.

Nitroimidazole radiopharmaceuticals for targeting hypoxia

AAmong various strategies to target tumor hypoxia, use of hypoxia activated prodrugs (HAPs) is most common. They are inactive compounds reduced selectively under hypoxic conditions by endogenously expressed oxido-reductases, resulting in the generation of an active compound. Among the hypoxia responsive molecules explored till date, 2-nitroimidazoles (NIs) and azobenzene (AB) derivatives are the most extensively exploited prodrugs for developing imaging agents. Nitroimidazoles undergo enzyme mediated selective reduction in hypoxic cells to form reactive products that irreversibly bind to cellular components [7]. Once within the intracellular environment, NIs undergoes nitroreductase enzyme mediated single electron reduction into RNO2 radical anion. This single electron reduction process is reversible and the radical anion generated in situ can undergo rapid re-oxidation to original NI in presence of intracellular oxygen, which has a higher electron affinity than the nitro group. After several such oxidation-reduction cycles, NIs eventually come out of tumor cells having normal oxygen partial pressure and cleared from the body. However, in hypoxic cells (pO_2<10 mmHg), absence/very limited availability of molecular oxygen drives the RNO_2 radical anion towards further reduction, eventually leading to covalent
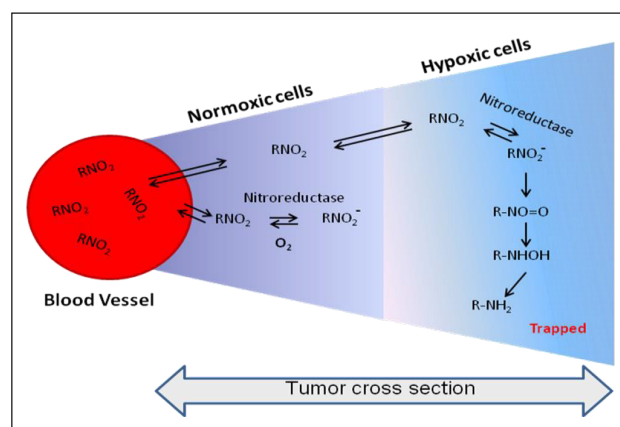

Figure 2. *Mechanism of oxygen dependent reduction of nitroimidazole in hypoxic cells*

binding to intracellular molecules in hypoxic cells. This mechanism forms the basis for using NI-based agents for selective targeting of hypoxic cells [Figure 2]. When radiolabeled with a suitable gamma emitting/ positron emitting radioisotope, NI-radiopharmaceuticals can be used to image spatial distribution of hypoxia in a tumor.

Recently, there has been significant interest to utilize nanoparticles for hypoxia imaging applications. Gold nanoparticles are extensively utilized for targeting cancer, exploiting its passive intra-tumoral accumulation through enhanced permeation and retention effect (EPR) as well as active uptake achieved via fictionalization. Facile surface chemistry, ease of synthesis, tunable size, low cytotoxicity and high adsorption capacity of gold nanoparticles offer effective tools to tailor pharmacokinetics for targeted applications [8]. Unique optical properties like surface plasmon resonance (SPR) has made gold nanoparticles preferred choice for developing agents for photothermal imaging, photothermal therapy and photodynamic therapy for cancer detection and cure [9]. Additionally, large surface-to-volume ratio of nanoparticles opens numerous possibilities from drug/radiosensitizer loading, surface modification with target specific biological vectors, tagging radioisotopes, etc.,

making them a multipurpose platform for developing targeted systems for drug delivery or radionuclidic therapy, either individually or in combination [10].[15–20]

[177]Lu-labeled gold nanoparticle for therapeutic dose delivery to hypoxic tumors

While mapping hypoxic region in tumor can help in hypoxia directed external beam radiation therapy, a prominent question is whether hypoxic cells can be mitigated by delivery of therapeutic dose of radiation through systemic administration of a hypoxia targeting therapeutic radiopharmaceutical. Towards this, a ^{177}Lu-labeled, nitroimidazole decorated gold nanoparticle was envisaged [Figure 3].

The gold nanoparticle provides the platform to hold the nitroimidazole moiety which would provide the hypoxia specificity while the macrocyclic chelator can be utilized to radiolabel with trivalent diagnostic radioisotope like gallium-68 or therapeutic radioisotope such as lutetium-177. The gold nanoparticle also provides an option to load radiosensitizers, chemotherapeutics or fluorescent tags, which could be used for optical imaging.
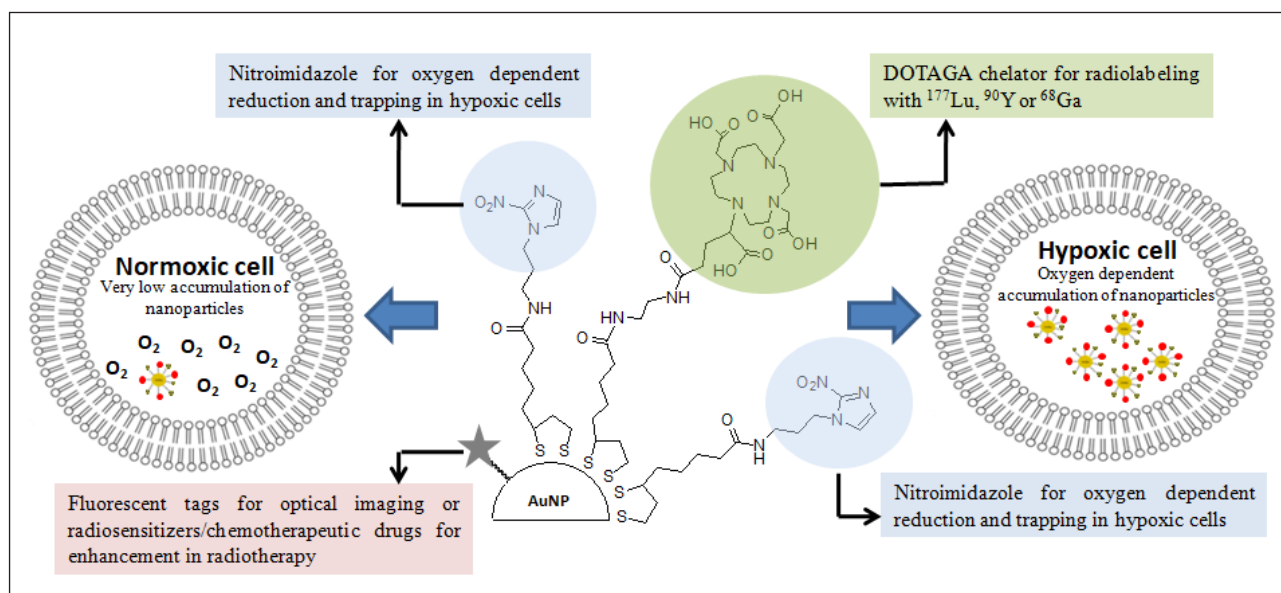

Figure 3. Conceptual design of nitroimidazole decorated gold nanoparticles for targeting tumor hypoxia

Synthesis

Various steps involved in the preparation of DOTAGA-conjugated, 2-nitroimidazole decorated gold nanoparticles are shown in Figure 4.

For facile attachment of 2-nitroimidazole to gold nanoparticles, 2-nitroimidazole (2-NIM) functionalized lipoic acid, NIM-TA (**3**) was synthesized by coupling 2-nitroimidazole amine (**2**) with lipoic acid [Figure 4(a)]. The 2-NIM tagged DOTAGA conjugated gold nanoparticles (DOTAGA-AuNP-2-NIM) were synthesized by in situ reduction of gold salt (HAuCl$_4$.3H$_2$O) with sodium borohydride (NaBH$_4$) [Figure 4(b)] in presence of excess of thiolated ligands, 2-NIM-TA (**3**) and DOTAGA-TA. The gold nanoparticles were purified by centrifugal filtration and characterized by DLS, UV-Vis spectroscopy, TEM, FT-IR and ^{1}H NMR spectroscopy. Evidence for the formation of gold nanoparticles could be obtained from the presence of typical SPR band at ~520 nm in UV-Vis spectrum. The DLS analysis showed DOTAGA-AuNP-2-NIM having effective hydrodynamic diameter of 60±1.5 nm [Figure 5 (a)]. The nanoparticles prepared displayed very low polydispersity index. Zeta potential of nanoparticles was found to be +20.22 mV at pH 7, indicating good suspension stability. The TEM images showed gold nanoparticles of uniform size, most of the particles in the range of 10–20 nm. Average particle size was 15±1.2 nm. Cyclic voltammetry of DOTAGA-AuNP-2-NIM (See ESI)[41] showed a peak at -1.21 V due to the reduction of nitro group in 2-nitroimidazole on the gold nanoparticle surface [Figure 5(a)], which closely matched with the first reduction peak in the cyclic voltammogram of free 2-nitroimidazole [not shown]. It is pertinent to note the absence of any reduction peak in the cyclic voltammogram of DOTAGA-AuNP without 2-NIM without 2-NIM decoration. This observation provided additional evidence for the presence of 2-nitroimidazole on the gold nanoparticle surface.

Lutetium-177 in chloride form (^{177}LuCl$_3$) is used for radiolabeling the functionalized gold nanoparticles. The radiochemical yield (RCY)
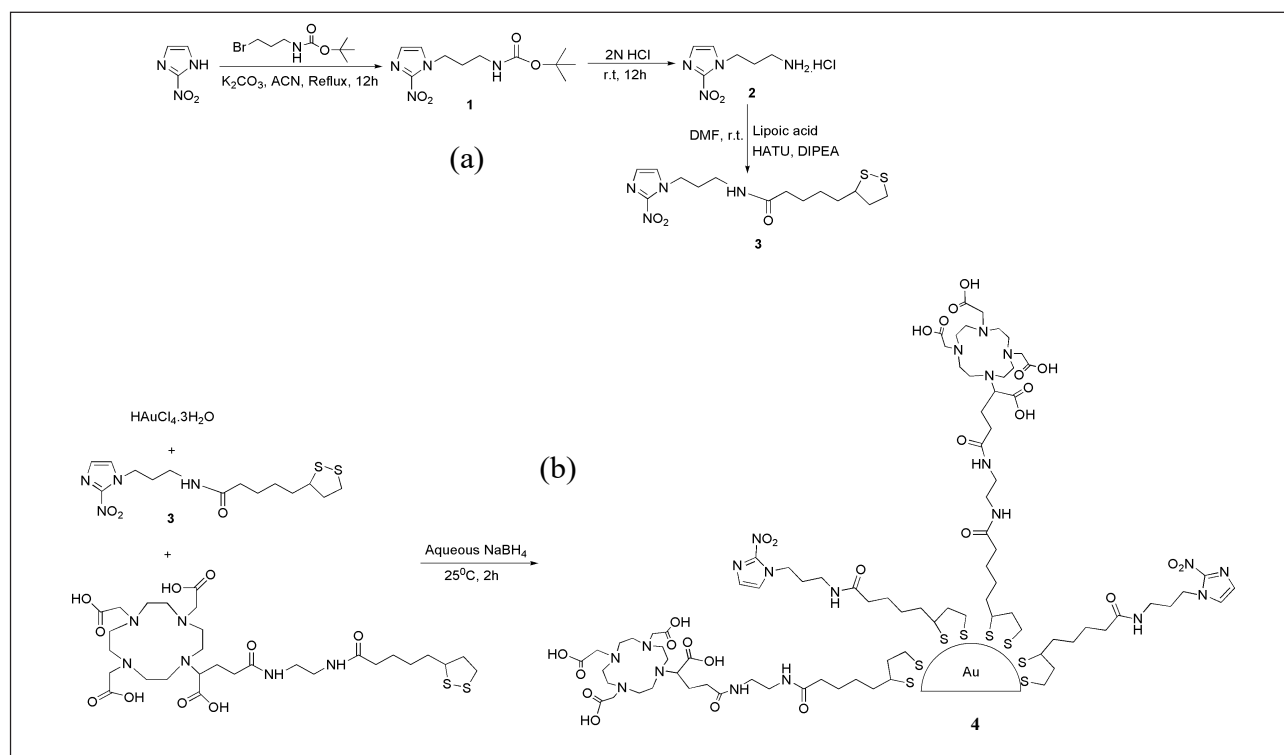

Figure 4. *(a) Synthesis of NIM-TA (**3**) (b) Synthesis of DOTAGA-AuNP-2-NIM (**4**)*
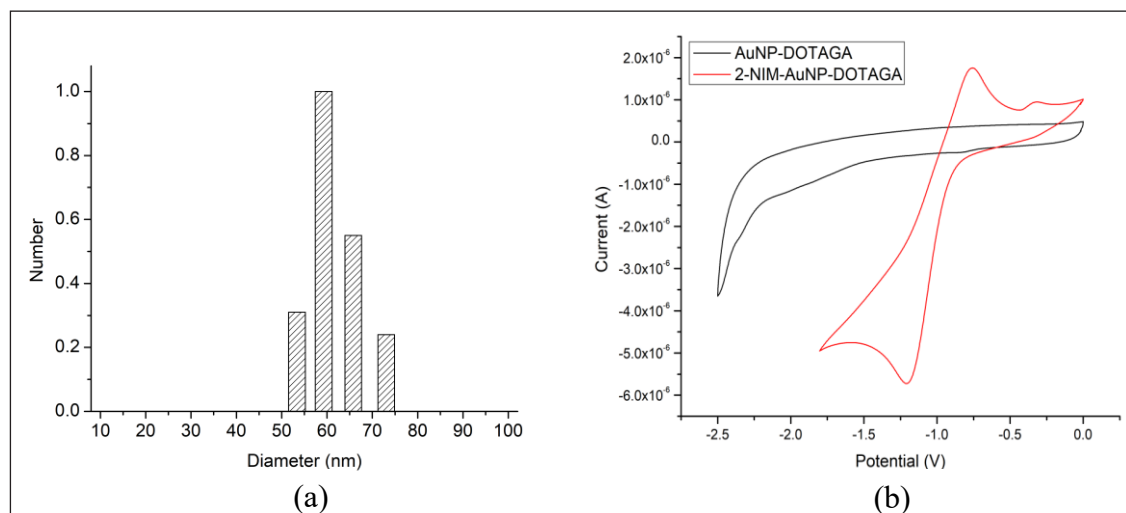
Figure 5. *(a) DLS plot of DOTAGA-AuNP-2-NIM and (b) Cyclic voltammogram of AuNP-DOTAGA and DOTAGA-AuNP-2-NIM*

and radiochemical purity (RCP) of [^{177}Lu]Lu-DOTAGA-AuNP-2-NIM was determined by size exclusion HPLC (SE-HPLC) [Figure 6]. Retention time of [^{177}Lu]Lu-DOTAGA-AuNP-2-NIM in HPLC was found to be 13.45±0.60 min [Figure 6(a)], whereas ^{177}LuCl$_3$ appeared at 22.19±0.40 min [Figure 6(c)]. From peak area measurements, RCY of [^{177}Lu]Lu-DOTAGA-AuNP-2-NIM was found to be above 90%. Bifunctional chelator used for surface modification of gold nanoparticles, DOTAGA, was radiolabeled separately for comparison. The peak corresponding to [^{177}Lu]Lu-DOTAGA appeared at 19.89±0.40 min [Figure 6(b)], distinctly different from the peak representing radiolabeled gold nanoparticle.

In-vitro studies were carried out in CHO cells under hypoxic and normoxic conditions to determine the hypoxia selectivity of [^{177}Lu]Lu-DOTAGA-AuNP-2-NIM. The uptake of radiotracer in CHO cells under hypoxic and normoxic condition is shown in Figure 7 (a) & (b). The results indicated significant uptake of radiotracer under hypoxic condition [Fig. 7(a)] compared to normoxic condition. The hypoxic/normoxic ratio for [^{177}Lu]Lu-DOTAGA-AuNP-2-NIM increased from 7.1 at 2h post-incubation (p. i.) to 9.2 at 4 h p. i. demonstrating excellent hypoxia selectivity. It is pertinent to note that
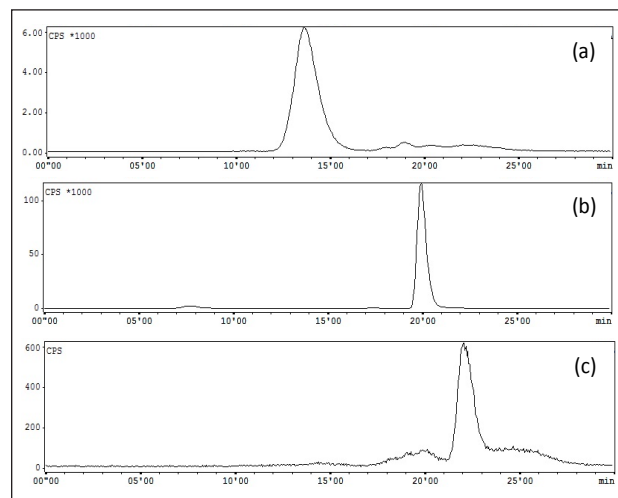
Figure 6. *Typical Size exclusion HPLC profiles (chromatogram) of (a) [^{177}Lu]Lu-DOTAGA-AuNP-2-NIM (b) [^{177}Lu]Lu-DOTAGA and (c) ^{177}LuCl$_3$*

[^{177}Lu]Lu-DOTAGA-AuNP without 2-NIM decoration showed very low cellular uptake under hypoxic as well as normoxic conditions [Fig. 7(b)].

Nitroimidazole mediated hypoxia selective internalization and accumulation of gold nanoparticles in CHO cell lines was further demonstrated using fluorescent nanoparticles, DOTAGA-AuNP(FITC)-2-NIM, synthesized following a protocol similar to the preparation of DOTAGA-AuNP-2-NIM. The fluorescent nanoparticles were incubated with CHO cells
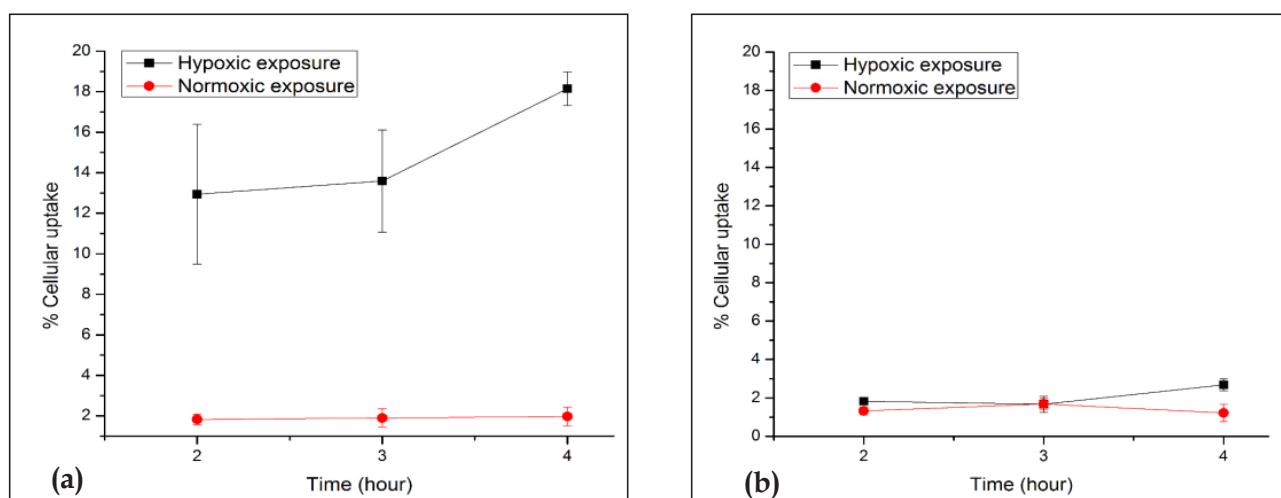
Figure 7. (a) Percentage cellular uptake of [^{177}Lu]Lu-DOTAGA-AuNP-2-NIM and (b) [^{177}Lu]Lu-DOTAGA-AuNP (Control) without 2-nitroimidazole moiety

under both hypoxic and normoxic conditions similar to the study using [^{177}Lu]Lu-DOTAGA-AuNP-2-NIM mentioned earlier. The cells acquired and analyzed using flow cytometer 24 h post incubation showed a strong fluorescent signal shift in the hypoxic group [~74.87% of cells with mean fluoscence intensity (MFI) of 3325.83±7.5 (pink)] indicating enhanced retention of DOTAGA-AuNP(FITC)-2-NIM under hypoxic condition as compared to normoxic condition [~79.15 % of cells with MFI of 45.22±8.56 (orange)] [Fig. 8] further confirming the role of 2-nitroimidazole in hypoxia specific accumulation.
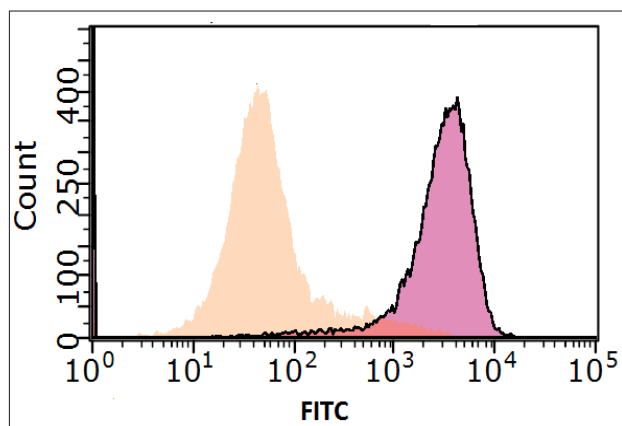
Figure 8*. FITC conjugated gold nanoparticles, DOTAGA-AuNP(FITC)-2-NIM, in CHO cells under normoxic and (Orange) and hypoxic (Pink) exposure*

Animal studies were conducted following the protocols approved by the Institutional Animal Ethics Committee. Biodistribution studies [^{177}Lu]Lu-DOTAGA-AuNP-2-NIM was carried out in Swiss mice bearing fibrosarcoma tumor. fast clearance of the nanoparticles could be observed from the animal body with ~70 % of the injected activity excreted within 3 h of injection. Similar observation was also reported for gallium-67 labeled bombesin conjugated gold nanoparticles [3]. Apparently, fast clearance has adversely affected the uptake and retention of the radiotracer in tumor. Generally nanoparticles reach tumor cells by passive diffusion driven by concentration gradient developed between blood pool and intracellular environment. Quick clearance of radiotracer from blood can reverse the concentration gradient resulting in poor distribution of the radiotracer in tumor and limited time available for the radiotracer undergo oxygen dependent reduction in tumor cells. However, it is pertinent to note that activity observed in tumor at 3h post-injection (p. i) is retained till 72 h p. i. indicating hypoxia specific reduction of the tracer in hypoxic tumor cells. Despite having very low uptake in tumor, the tumor to blood ratio and tumor to muscle ratio progressively increased with time owing to clearance of radiotracer from blood as well as muscles.

Conclusions

The DOTAGA-AuNP-2-NIM is a potential hypoxia targeting platform which can be loaded with fluorescent markers, diagnostic radioisotopes, radiosensitizers or potent therapeutic radioisotopes for multimodal imaging of hypoxia or radiosensitizer enhanced hypoxia directed internal radiotherapy. Though the in vitro studies demonstrated excellent accumulation of [^{177}Lu]Lu-DOTAGA-AuNP-2-NIM nanoparticles in CHO cells under hypoxic conditions, further improvement is required in its pharmacokinetics.

Acknowledgement

Reference

1. Vaupel, P.; Flood, A. B.; Swartz, H. M. Oxygenation Status of Malignant Tumors vs. Normal Tissues: Critical Evaluation and Updated Data Source Based on Direct Measurements with PO2 Microsensors. *Appl Magn Reson* **2021**, *52* (10), 1451–1479.

2. Colliez, F.; Gallez, B.; Jordan, B. F. Assessing Tumor Oxygenation for Predicting Outcome in Radiation Oncology: A Review of Studies Correlating Tumor Hypoxic Status and Outcome in the Preclinical and Clinical Settings. *Front. Oncol.* **2017**, *7*.

3. Kumari, R.; Sunil, D.; Ningthoujam, R. S. Naphthalimides in Fluorescent Imaging of Tumor Hypoxia – An up-to-Date Review. *Bioorganic Chemistry* **2019**, *88*, 102979.

4. Dewhirst, M. W.; Cao, Y.; Moeller, B. Cycling Hypoxia and Free Radicals Regulate Angiogenesis and Radiotherapy Response. *Nat Rev Cancer* **2008**, *8* (6), 425–437.

5. Liu, J.; Bu, W.; Shi, J. Chemical Design and Synthesis of Functionalized Probes for Imaging and Treating Tumor Hypoxia. *Chem. Rev.* **2017**, *117* (9), 6160–6224.

6. Waller, J.; Onderdonk, B.; Flood, A.; Swartz, H.; Shah, J.; Shah, A.; Aydogan, B.; Halpern, H.; Hasan, Y. The Clinical Utility of Imaging Methods Used to Measure Hypoxia in Cervical Cancer. *BJR* **2020**, *93* (1111), 20190640.

7. Rashed, F. B.; Diaz-Dussan, D.; Mashayekhi, F.; Macdonald, D.; Nation, P. N.; Yang, X.-H.; Sokhi, S.; Stoica, A. C.; El-Saidi, H.; Ricardo, C.; Narain, R.; Ismail, I. H.; Wiebe, L. I.; Kumar, P.; Weinfeld, M. Cellular Mechanism of Action of 2-Nitroimidazoles as Hypoxia-Selective Therapeutic Agents. *Redox Biology* **2022**, *52*, 102300. https://doi.org/10.1016/j.redox.2022.102300.

8. Gray, L. H.; Conger, A. D.; Ebert, M.; Hornsey, S.; Scott, O. C. The Concentration of Oxygen Dissolved in Tissues at the Time of Irradiation as a Factor in Radiotherapy. *Br J Radiol* **1953**, *26* (312), 638–648. https://doi.org/10.1259/0007-1285-26-312-638.

9. M. R. K. Ali, Y. Wu and M. A. El-Sayed, *J. Phys. Chem. C*, 2019, **123**, 15375–15393.

10. Overgaard, J. Hypoxic Modification of Radiotherapy in Squamous Cell Carcinoma of the Head and Neck--a Systematic Review and Meta-Analysis. *Radiother Oncol* **2011**, *100* (1), 22–32.

Dr. Madhava B Mallia *is presently the Head of Radiopharmaceuticals Chemistry Section in Radiopharmaceuticals Division of Bhabha Atomic Research Centre, Mumbai. He completed his MSc in Applied chemistry from Cochin University of Science and Technology. After a brief stint in National Chemical Laboratory, Pune, he joined BARC Training School in 2001. He was awarded with Homi Bhabha gold medal for securing 1st rank in BARC Training School in Chemistry discipline. In 2002, after successful completion of the training program, he joined Radiopharmaceuticals Division, BARC. His main area of research is the development of Technetium-99m-tracers, with small biomolecules, antibodies and peptides as targeting vectors, for diagnosis, with a possible extension of the idea to corresponding rhenium-186/188 analogues for therapy. He has over 50 research articles in various peer reviewed journals and he is also the recipient of the DAE-Scientific and Technical Excellence Award (2015) and Dr. Tarun Datta Memorial Award (2019). He served as subject expert for Regional Training Program of IAEA in Thailand (2018) and participated as consultant for IAEA Technical Meeting on New Generation of Technetium-99m kits (2021, 2022).*

Sweety Mittal is working as Scientific Officer at Bhabha Atomic Research Centre, Mumbai, India. She obtained her Doctor of Philosophy degree(PhD) in 2009 from Indian Institute of Technology (IIT) Roorkee India. After that she joined BARC in July 2011 as a Scientific Officer D. Her expertise lies in Synthetic organic Chemistry and Radiopharmaceuticals Chemistry. Her primary area of research is the development of radiopharmaceuticals for hypoxia imaging and preparation of new nanoplatforms for radiopharmaceutical applications, including for targeting tumor hypoxia.

Dr Rohit Sharma *Joined BARC as part of the 58th Batch of the OCES program. He has the expertise in the development of antibody and peptide based diagnostic and therapeutic radiopharmaceuticals, with a focus on advancing both clinical and scientific applications of radiopharmacy. With over 35 publications in peer-reviewed journals, his research aims to enhance the effectiveness of radiotracers for medical diagnostics and targeted therapies. He was also conferred with the Young Scientist Award by the Society of Radiation Research for his contributions to this field. Additionally, he received travel grant from SERB DST and King's College London to participate in international scientific conferences.*

Radiation as a tool for synthesis of Polymers, Hydrogels and Nanofibers

J. K. Ajish

Radiation and Photochemistry Division, Bhabha Atomic Research Centre,
Trombay, Mumbai 400085
E-mail: kuttan@barc.gov.in

Abstract

Radiation induced techniques for making new materials and for modification of existing materials to introduce desired properties have received more acceptance these days industrially. Being a green, clean and easily scalable technique is one of the major benefits of radiation technology. A lot of fundamental studies have been carried out in the field of radiation chemistry which is the building blocks for many of the radiation induced industrial processes. In this article emphasis is laid on the synthesis of biomaterials like silver nanoparticle loaded hydrogels for wound dressing applications, glycopolymeric hydrogels as well as gel microspheres and electrospun nanofibers for targeted drug delivery utilizing ionizing radiation.

Introduction

Radiation technology for synthesis of various polymeric systems have made significant development, that many of them have reached industrial application stage [1]. Ionizing radiation induced processes are used for synthesis of new polymers and to modify the properties of existing polymers. New polymeric materials can be synthesized by radiation induced polymerization, radiation induced gelation and radiation induced synthesis of nanoparticles as well as nanogels.

Modification of polymers as per the requirement can be done efficiently using high energy radiation like gamma rays, X rays, electron beams, ion beams etc. Irradiation of polymers leads to formation of intermediates which can be in the form of excites state species, ions and free radicals. These highly reactive intermediates immediately get used up in the formation of oxidized products, grafted chains, crosslinking or chain scission of the polymer leading to degradation. The dominance of any particular pathway in which intermediate species react depend on the nature of the polymer as well as the pre and post irradiation conditions. These parameters can be controlled precisely making modification of polymers feasible by irradiation.

Radiation based techniques have many advantages over conventional polymerization processes. Firstly, radiation processing does not involve use of any catalysts or initiators as additives. The energy of the incident radiation is utilized for initializing polymerization via a free radical pathway. It has been observed that same number of initiating radicals are produced during 1 rad/s dose rate radiation dose exposure or chemical initiators like benzoyl peroxide at 0.1M concentration. Radiation induced reaction initiation have advantages that it is cleaner because the concentration and purity of chemical initiators need not be considered, dose rate can be varied easily, it is a temperature independent process therefore it requires zero activation energy for initiation.

Radiation crosslinking is a widely used technology in wire and cable industry, heat-shrinkable packaging film production, tubings and foam production etc [2]. Automobile tyres are manufactured using radiation crosslinked rubber strips. Radiation curing is industrially used for large scale production of surface finished coatings and inks [3]. Radiation degradation also finds application in increasing solubility of certain polymers such as Teflon for use as fillers

in various applications [4]. Radiation grafting is yet another technique for modification of polymers for enormous range of applications. The production of battery separators from acrylic acid grafted polyethylene is one of the major examples of industrial scale radiation grafting.

Radiation induced techniques helps to carry out on-site manufacturing processes in hard-to-reach places. In addition, we get a radiation sterilized product which can be used directly for bio medical processes. The following are the disadvantages of radiation induced method of initiation:

1) Stringent safety requirements in the areas where ionizing radiation is applied

2) Possibility of occurrence of side reactions in the presence of ionizing radiation.

These disadvantages can be easily eliminated by suitable safety engineering and by selection of optimum polymerization conditions.

Polymers can be classified as radiation degrading and radiation crosslinking type based on the stability of polymeric chains to ionizing radiation [5]. This may sound little oversimplified, because any advantageous crosslinking process involves some degree of degradation which we have to deal with. PTFE is a well-known radiation degrading type polymer but it can be crosslinked in molten state at 340°C, under argon atmosphere at low dose rate [6].

Radical polymerization induced by gamma irradiation

Synthesis of hydrogels by radiation initiation can be made possible by exposing vinyl monomers to ionizing radiation in aqueous media. The radiolysis of water leads to formation of radicals which initiates the polymerization. The main reactive species generated in water upon irradiation are hydroxyl radicals, hydrated electrons and hydrogen radicals. Hydrated electron exhibits very weak direct interaction. It rather interacts with water molecules leading to generation of $\cdot$H and $\cdot$OH radicals. The $\cdot$H radicals recombine to give H_2 gas. The main reactive species $\cdot$OH are responsible for polymerization processes. It abstracts hydrogen from the C-H bond in polymeric chain leading to formation of macroradicals (C$\cdot$). These macroradicals crosslink to form crosslinked hydrogels or polymer [7].

For wound dressing applications, hydrogels are made with polymers like polyvinylalcohol (PVA) which are crosslinking in nature. Introduction of natural polysaccharides into these hydrogels increases the water retention capacity of the hydrogels and improves the flow properties suitable for application on the wound [8, 9, 10, 11]. Natural polysaccharides as such are radiation degrading but in combination with PVA like systems the extent of degradation is drastically reduced. In this context we have synthesized antibacterial PVA-gum acacia-based hydrogel with insitu formed AgNPs, for wound dressing applications (Figure 1) [12].

Equation 1 and 2 depicts the role of .OH radicals in crosslinking PVA polymeric chains.

$$PVA(H) + OH^{\bullet} \rightarrow PVA^{\bullet} + H_2O \text{ -------- (1)}$$

$$2PVA^{\bullet} PVA \rightarrow PVA \text{ (crosslinked polymer) -(2)}$$

Insitu generation of AgNPs in a crosslinked hydrogel can be explained as follows. Ag^+ ions are known to have very high reactivity with both hydrated electrons (k = 4.8 x 10^{10} dm^3 $mol^{-1}s^{-1}$) and hydroxyl radicals (k = 9.7 x 10^9 dm^3 $mol^{-1}s^{-1}$). But the hydroxyl radicals preferentially react with PVA as shown in equation 2 and hence the reduction of Ag^+ ions takes place by the strongly reducing radicals in the medium i.e hydrated electron and polymeric radical PVA which was formed as per equation 2.

$$nAg^+ + e^-_{aq}/PVA^{\bullet} \rightarrow (Ag)_n \text{ (Ag clusters) ----- (4)}$$
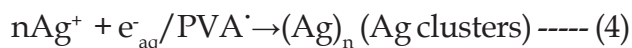
When we irradiate aqueous solutions saturated with N_2O, the hydrated electrons are converted to oxidising species i.e hydroxyl radical as shown in equation 3. These hydroxyl radicals are utilized to exclusively convert PVA to PVA radicals which further reduces the Ag^+ ions.

$$N_2O + e^-_{aq} \rightarrow {}^{\bullet}OH + N_2 + OH^- \text{ ---------------- (3)}$$
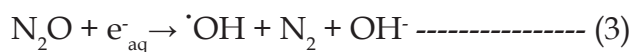
Figure 1: Radiation induced synthesis of AgNPs loaded PVA- gum acacia based hydrogel

The hydrogel was synthesized at a radiation dose of 32 KGy which not only crosslinks the system, but also sterilizes and reduces the silver precursor to AgNPs. The antibacterial activity against *E.coli* bacteria indicated that smaller the size of the AgNPs better is the antibacterial activity (Figure 2).

Glycopolymer gel stabilized N-succinyl chitosan microsphere for controlled anticancer drug delivery

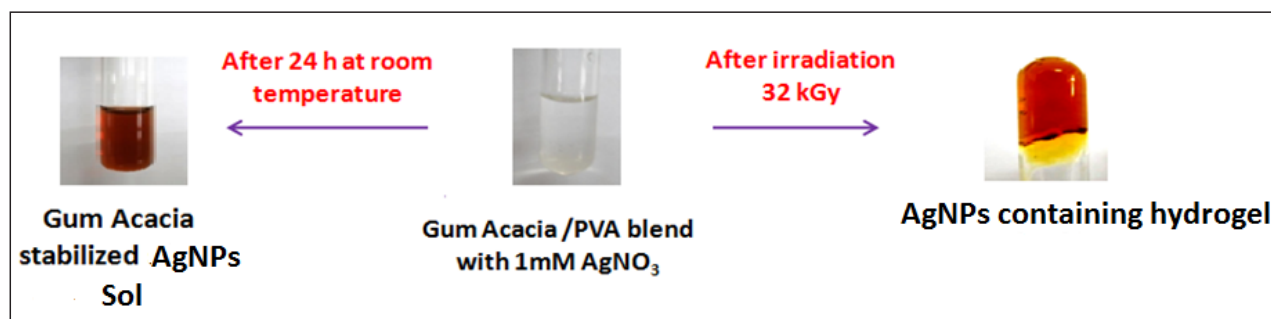Controlled anticancer drug delivery is an important research area inorder to increase the activity of drug with least toxicity to healthy cells. Sugar based polymers like glycopolymers act as drug carriers where the sugar pendants act as pilot molecules. Sugars play significant role in cellular biorecognition events thus facilitating targeted deliver of the drug [13]. It is

well established that sustained release of drug at the malicious site is more effective for tumor treatment than the administration of drug in definite doses at specific intervals.

Keeping these points in mind we have designed and synthesized a glycopolymer stabilized $N-$succinyl chitosan (NSC) gel microsphere (Glc-gel) which was loaded with anticancer drug Doxorubicin. The calcium ion crosslinked NSC microsphere was stabilized mechanically by irradiating it with the glucose acrylamide monomer and glucose bisacrylamide crosslinker in a Co-60 gamma source upto atotal dose of 1.68 kGy @ 0.75 kGy/h [14,15]. This led to the formation of an interpenetrating glycopolymeric network in the microsphere (Figure 3). This was loaded with the drug and
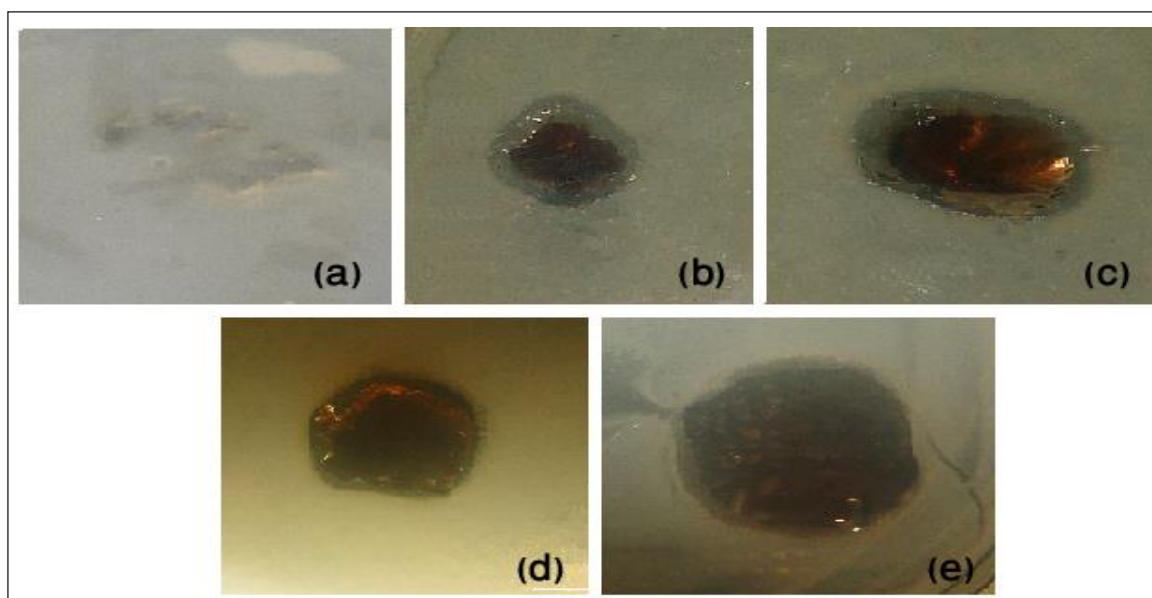

Figure 2: Antibacterial activity of AgNPs loaded hydrogel against E.coli bacteria with varying gum acacia concentration.

further studies were carried out. Also, the cell cytotoxicity studies using L929 and INT407 cell lines by MTT assay of Glc-acryl, Glc-bis as well as the Glc-gel did not show any significant difference between the untreated and treated samples.These results clearly indicated that Glc-acryl and Glc-bis as well as Glc-gelwere not toxic to the cells.
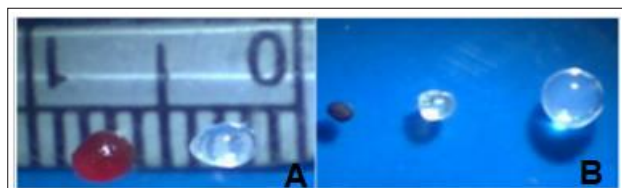

Figure 3: (A) DOX loaded and unloaded radiation crosslinked glycopolymeric microsphere (B) Radiation crosslinked glycopolymeric microspheres in dried and swollen form (C) Swelling behaviorsof Glc-gel at pHs 3, 5 and 7.4.

The DOX encapsulation efficiency (EE) of the beads was dependent on the degrees of succinylation in the NSCs. Quantification of the data revealed that the EEs of the 80% succinylated and 67% succinylatedGlc-gel beads were 92.7% and 75% respectively. This suggested that the mechanism of loading is governed mainly by the electrostatic interaction between the –COO⁻ groups in the polymer and the NH_2 group of DOX.

The DOX loaded microspheres exhibited pH dependent delivery of the drug in a slow and sustained manner. About 88% of the loaded drug
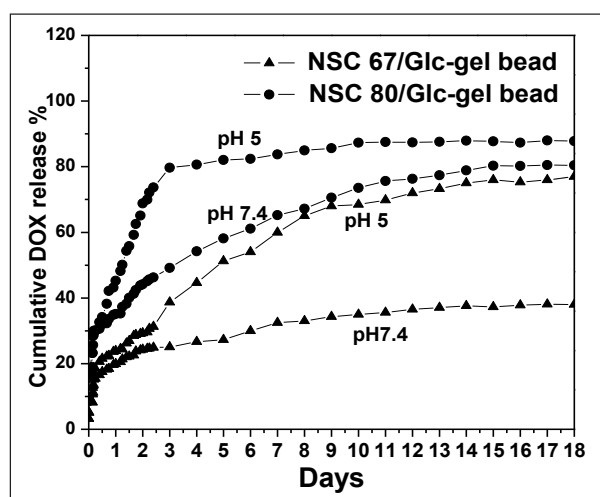
Figure 4:DOX release profiles from the loaded NSC/Glc-gel beadsat pHs 7.4 and 5.

was released over a period of 18 days (Figure 4). This system finds application in implants or post-surgical treatment of localized cancer.

Radiation crosslinked electrospun nanofibers

Nanocarriers are well known for anticancer drug delivery but they have many limitations like overcoming the mucosal barriers to cancer cells, lack of specificity, low loading efficiency of drug etc. Also the intravenously injected nanocarriers will be inevitably distributed to healthy cells in addition to cancer cells leads to added toxicity. These factors make nanocarriers far from clinical applications [16].

The above mentioned problems can be solved by utilizing localized drug delivery which will ensure the required concentration of drug specifically at the cancer cell site, provides more residence time for the drug action and reduced systemic toxicity.Electrospun nanofibers are excellent drug carriers with high drug encapsulation efficiency, high specific area and volume. We have synthesized a core-shell electrospun nanofiber with drug loaded polysaccharide as the core and galactosylated PVA as the shell. Radiation induced crosslinking was used for making the shell layer keeping the core layer intact. The nanofibers are being tested for targeted drug delivery to liver hepatocytes.

Figure 5: (A) Core shell electrospinning setup (B) Insitu UV-polymerization with electrospinning

The core-shell nanofibres prepared by coaxial electrospinning (Figure 5) method facilitates continuous release of drugs from the nanofibres without any burst release. The core shell nanofibres not only reduces burst release of the drug but also protects the drug loaded core layer. The high cytotoxicity of anticancer agents during localized drug delivery is reduced in case of core shell nanofibres compared to the pr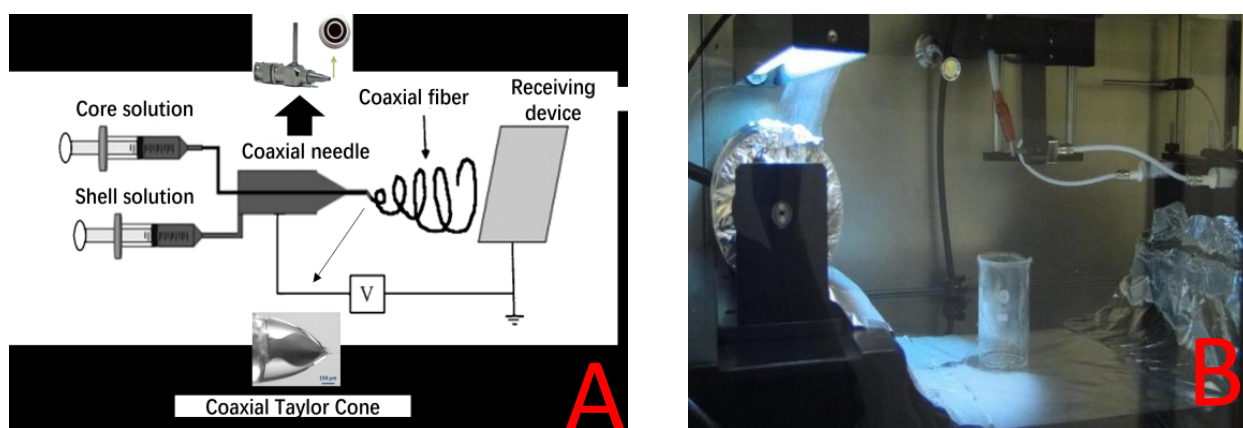istine anticancer drugs like Doxorubicin (DOX), folic acid, paclitaxel, 5-fluoruracil etc. The anticancer drugs are incorporated into the core layer which is composed of hydrophilic polymers like polyvinyl alcohol (PVA), polyethylene oxide, gelatine, chitosan and its derivatives. Chitosan is a natural polymer with many favourable properties like biocompatibility, biodegradability, low cost etc. But its application in drug delivery systems is limited due to its poor solubility under body fluid conditions. Hence we have used *N*-succinylated chitosan (NSC) as the core layer for loading DOX. NSC with more than 80% succinylation is easily soluble in body fluid conditions (pH 7.4) and can be used to load DOX.HCl electrostatically. The shell layer is a copolymer of PVA-Glycidylmethacrylate (GMA) and galactose acrylamide (Gal-acryl), which was crosslinked by radiation polymerization. The galactose functionality on the surface is used for liver specific targeted drug delivery due to its affinity to asialoglycoprotein receptors (ASGP-R).

The loading of DOX was confirmed by the change in zeta potential of the Gal-PVA@NSC from -30 mV to 0.1 mV. The DOX is loaded in to the core N-succinylated chitosan by electrostatic interaction between NSC and DOX.HCl. The encapsulation efficiency of DOX was calculated to be 34.8% at 1:1 ratio of [NF]/[DOX]. DOX release studies indicate 32% drug release at pH 5 and only 22% drug release at pH 7.4after 10 hours. This further confirms slow and sustained delivery of the drug with minimum side effects to the healthy cells than cancer cells.

Conclusion

This article emphasizes on the use of ionizing radiation as an efficient source of initiation for polymerization, crosslinking and curing of materials. It can be used as an alternative to thermal initiators like peroxides under modest heating conditions. The thermal activation of the polymeric chains during conventional initiation processes can be decoupled during radiation induced processes thus avoiding the effect on chain length of formed polymers. Radiation processing of polymers is a fast, clean, reliable, reproducible and upscalable technology. It can find application in industry, healthcare, agriculture and environment. With increasing demand for new materials and greener technologies, radiation-based techniques are expected to grow further at a faster pace in the coming years.

References

1. R.L.Clough, Nucl. Instrum. Methods Phys. Res.B. 185 (2001) 8.
2. T. Seguchi, T. Yagi, S. Ishikawa and Y. Sano, Rad. Phys. Chem. 63 (2002) 35.
3. J.V. Crivello, Rad. Phys. Chem. 63 (2002)21.
4. C. V. Chaudhari, K. A. Dubey and Y. K. Bhardwaj, in"Applications of High Energy Radiations. Materials Horizons: From Nature to Nanomaterials", S. R. Chowdhury, Ed; Springer, Singapore (2002) 7.
5. International Atomic Energy Agency Consultants Meeting: Radiation in degrading natural and synthetic polymers, Rio de Janeiro, Brazil, 7–9 August, 2002.
6. T. Yamaki, M. Asano et al., Rad. Phys. Chem. 67 (2003),403.
7. M. M. Ghobashy, in "Ionizing Radiation Effects and Applications", B. Djezzar, Ed; IntechOpen (2018) 28.
8. V. K. Sharma, R. A. Yongard and Lin, Y. Adv. Colloid Interface Sci. 145(2009)83.
9. H. Kong andJ. Jang, Langmuir. 24(2008) 2051.
10. V. Thomas, M. Namdeo, Y. M. Mohan, S. K. Bajpai and M. Bajpai,J. Macromol. Sci., Part A: Pure Appl. Chem. 45 (2008) 107.
11. V. Thomas, Y. M. Mohan, B. Sreedhar and S. K. Bajpai,J. Biomater. Sci. Polym. 20 (2009) 2129.
12. K. A. Juby, C. Dwivedi, S. Kota, M. Kumar, H.S. Mishra and P.N.Bajaj, Carbohydr. Polym. 89 (2012)906.
13. H. Freichels, R. Jerome and C. Jerome,Carbohydr. Polym. 86(2011) 1093.
14. J. K. Ajish, K. S. A. Kumar, S. Chattopadhyay, M. Kumar, Carbohydr. Polym. 144 (2016) 98.
15. J. K. Ajish, K. S. A. Kumar, M. Subramanian and M. Kumar, RSC Adv. 4 (2014) 59370.
16. J. Xue, T. Wu, Y. Dai, and Y. Xia, Chem. Rev. 119 (2019) 5298.

Juby K. Ajishjoined Bhabha Atomic Research Centre in 2010 after graduating from 53rd batch of BARC training school. She obtained her MSc from Calicut University in 2008. She obtained her Ph.D. from Homi Bhabha National Institute, Mumbai, India in 2016, for her work on "Synthesis and study of carbohydrate-based hydrogels for biomedical applications". She is currently working on many important DAE relevant projects apart from directed research in the field of polymer chemistry.Her research interest includes fabrication of plastic scintillators and thin films for radiation detection, synthesis of polymeric hydrogels for various biomedical applications, utilization of synthetic polymers and functionalization of natural polymers for targeted drug delivery applications, synthesis and applications of glycopolymers in lectin recognition and bacterial detection.She has 25 publications in reputed journals with 507 citations and 3 technical reports to her credit.

Evaluating the Qualitative and Quantitative Analysis of a Drug in Pharmaceutical Formulations Using Steady-State and Time-ResolvedSpectroscopy

Dineshbabu Takkella [a], Krishna Gavvala [a*]

[a]Department of Chemistry, Indian Institute of Technology Hyderabad, Kandi, Sangareddy, Telangana 502284, India

*(email: kgavvala@chy.iith.ac.in)*

Abstract

Herein, we performed the quantitativeand qualitative analysis of Imiquimod (IMQ), well-known antiviral and anticancer drug, present in the commercially available cream asimiquad sachet(aldara). Imiquad cream was first analyzed in water, methanol, and 0.05M NaOH to quantify the IMQ drug in its multiple conformations. The limit of detection (LOD) and quantitation (LOQ) were measured using absorption and fluorescence methods. The fluorescence technique (~0.06 μg/mL) is found to be more sensitive for drug quantification, with alowerLOD than the absorption measurement (~0.6 μg/mL).Qualitative analysis was performed using the Time-Correlated Single Photon Counting (TCSPC) technique andmonitored the excited-state properties of the molecule. The lifetime components of the imiquad creamclosely aligned with the standard IMQ values, confirming the purity/quality of IMQ.This indicates that the placebo and stabilizers in the formulation did not interfere with the IMQ drug. Quantification and qualitative analysis are very crucial for any drug as they are closely linked to patient health and the threat of counterfeit drugs.Therefore, the methodologies developed here can find potential applications in the pharmaceutical sector.

Introduction

The pharmaceutical analysis is an important research area to regulate drug compound identification, strength, quality, and concentration.[1]Particularly, quality test analysis of any drug is vital before evaluating the patient's health.[2]On the other hand,determination pfthe quantity of pharmaceuticals can be done using UV visible spectrophotometry as most drugs have chromophores in their structure.[3]Spectroscopy is most commonly used tool for quantitative analysis because the measurements involve less expensive with lower maintenance issues[-1] There are other robust techniques, such as XRD, chromatography, etc., available to determine the quantity/quality; however, UV-VIS spectrophotometry and spectrofluorometer methods are commonly available, easier to use, highly reliable, and highly accurate owing to their ultrasensitive nature.[4, 5]Since numerous pharmaceutical substances exhibit fluorescence, they can be explicitly determined.If the substance is a non-fluorescentthey can still be quantified using fluorescence spectrophotometry bysynthesizing their fluorescent products.[6]Herein, we have used combination of steady-state and time-resolved fluorescence based tools to determine the quantitative and qualitative analysis of a drug. For the first time, we used a technique based
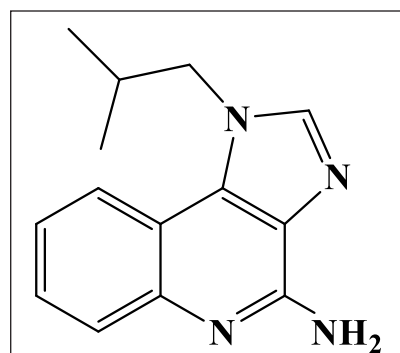
Scheme1.*Molecular structureof imiquimod (IMQ).*

onthe time-correlated single photon counting (TCSPC) principle for the qualitative analysis of drugs.

In the present work onqualitative and quantitative analysis we have chosen a drug,IMQ (**Scheme 1**),with antiviral and antitumor properties.The mechanism of the drugistoactivate TLR-8, TLR-7, and toinduce tumor necrosis factor α (TNF-α), interferon-α (INF-α).[7-10]The US Food and Drug Administration (FDA) approved imiquimod in a 5% formulation, commercially known as Aldaracream(Imiquad cream), for the treatment of actinic keratosis, superficial basal cell carcinoma, external genital warts caused by HPV, metastatic melanoma, and molluscum contagiosum in children.[11-16]Photophysical studies on this IMQ drug remain scarce despite their potential for skin-based medications, which are more likely to be exposed to light. Recently, we have explored the excited-state dynamics of IMQ in both aqueous solutions, organic solvents, and its binding interactions with DNA, providing valuable insights into its photophysical behavior.[17-19]It was observed that the IMQ exists in different formsin both the ground and excited states based on the surrounding environment, such as cation, neutral, tautomer, and anionic forms depending upon the pH and solvent of the medium.[17, 18]IMQ exhibits a unique rise component in its lifetime at pH > 11 when measured at an emission wavelength of 425 nm, implying unique excited-state dynamics.[18]Such unique fluorescence properties of the drug motivated us to use themfor quantity and quality analysis.However, no such study has been conducted on the quantitative and qualitative analysis of IMQ in imiquad creamusing fluorescence methods, which are more accurate. IMQ exists as different conformers based on pH and polarity of the medium. Hence, we have used methanol, water, and 0.05M NaOH to analyze the differentconformations of IMQ drug in a commercially available imiquad sachet. Fluorescencelifetime feature has been monitored to evaluate the quality of the drug present in the commercially available sachet. Moreover, the drug quantity in theimiquad sachet is established using UV-VIS absorption and fluorescence studies. Fluorescence lifetime-based analysis for quality assessment of the drug may significantly enhance the quality control of pharmaceutical formulations.

Experimental section

IMQ (purity >98%) was bought from TCI Chemicals and used without further purification. Imiquad sachets (5% w/w) werepurchased from Glenmark Pharmaceuticals, Goa. Methanol (HPLC grade) was sourced from Thermo Fisher Scientific. Deionized water and NaOH pellets (>98%, Srichem) were used to make a 0.05 M NaOH solution. The imiquad cream was dissolved in 60 mL of methanol and sonicated for 30 minutes to make the imiquad cream stock solution. After sonication, the solution was purified using Whatman 41 filter paper and diluted to 100 mL with methanol. UV absorption spectra were measured using a Jasco V-730 spectrophotometer,and fluorescence emission spectra were measured on a HORIBAFluoroMax4spectrofluorometer. Time-resolved fluorescence studies were conducted using a time-correlated single-photon counting (TCSPC) technique (Horiba FluoroHub) with an instrumental response function (IRF) of ~1 ns. Excitation was achieved using a NanoLED with a wavelength of 291 nm and a pulse duration of 1 ns, operating at a repetition rate of 1 MHz. TCSPC data were analyzed and fitted with the DAS6 software using a multiexponential decay model (**1**).[20]

$$f(t) = \sum_{i=1}^{n} \alpha_i e^{-t/\tau_i} + \varepsilon(t \geq 0) \quad (1)$$

Here, f(t) represents the overall fluorescence decay, with n distinct components. Each component is indicated by a lifetime t_i and its fractional amplitude a_i. The fractional amplitudes $a_1 + a_2 + \dots$, are normalized to 1, andεdescribes for additional noise. A reliable fit was concluded by monitoring residuals and ensuring a χ^2 value close to 1.

16

Results and discussion

Quantitative analysis of IMQ

To quantify the IMQ in the imiquad cream, the absorption and emission spectra of standard IMQ at different concentrations (0.6–1.5 µg/mL) were analyzed to construct a calibration plot. Using the calibration procedure, the unknown concentration of IMQ in an Imiquad cream was determined based on its absorption and fluorescence spectra in methanol, water, and 0.05M NaOH, as illustrated in **Figure 1**. The characteristic peaks of both the absorption and emission spectra of standard IMQ in aqueous and organic solvents are consistent with findings from our previous work.[17, 18] The IMQ molecule can exist in neutral, tautomeric, cationic, and anionic forms, depending on the surrounding medium. In the case of neutral pH (water), IMQ exists as cationic, neutral, and tautomeric forms.[17, 18] In methanol, IMQ predominantly adopts tautomeric and neutral forms. In contrast, under basic conditions (0.05 M NaOH), IMQ primarily exists in the anionic form.[17, 18] The spectral profile of the IMQ in imiquad sachet cream perfectly matches with the characteristic features of the standard IMQ spectra (**Figure 1**).

Standard calibration curves were plotted by recording absorption and emission spectra of standard IMQ at various concentrations (0.60-1.5 µg/ml) in methanol, 0.05M NaOH, and water, as shown in the inset images of **Figure 1**. The calibration method was used to determine the exact concentration of the IMQ drug present in the commercial cream. The smallest amount of analyte in a sample that can be detected is called the limit of detection (LOD). The limit of quantification (LOQ) is the smallest amount of analyte in a sample that can be quantified. LOD and LOQ were determined using equations **(2)** and **(3)**.

$$LOD = 3.3\sigma/S \qquad (2)$$

$$LOQ = 10\sigma/S \qquad (3)$$

where S is the slope of the relevant calibration curve, and σ is the standard deviation of the response.[21] The recovery percentage was calculated using the equation **(4)**

$$\% \text{ of Recovery} = \frac{\text{Amount Found} \times 100}{\text{Amount Added}} \quad (4)$$

The recovery analysis of the IMQ using the spectrophotometric and spectrofluorometer methods, as shown in **Table 1,** gives the determination coefficient (R^2) values in methanol, water, and 0.05M NaOH, respectively. R^2 values ~1 indicate a good relationship between concentrations of IMQ and respective absorbance and fluorescence emission. The recovery percentage (**equation 3**) of the drug from the sachet was calculated (**Table 1**) in methanol, water, and 0.05 M NaOH within the allowed 15% limit by International Council of Harmonization (ICH) guidelines.[22]

The limit of detection (LOD) and quantification (LOQ) values were calculated (**equations 1 & 2**) using absorbance and fluorescence intensity, as shown in **Table 2.** The LOD values from absorbance are 0.153 µg/ml, 0.756 µg/ml, and 0.537 µg/ml in methanol, water, and 0.05M NaOH, respectively. On the other hand, the limit of detection values from fluorescence were calculated to be 0.063 µg/ml, 0.067 µg/ml, 0.065 µg/ml, and 0.056 µg/ml in methanol, water, and 0.05M NaOH at 350 nm and 425 nm, respectively. By comparing both methods, the spectrofluorometric technique returned values 10 times lower, highlighting its superior sensitivity over the spectrophotometric method. The LOQ values from the spectrophotometric method were 0.463 µg/ml, 2.293 µg/ml, and 1.628 µg/ml in methanol, water, and 0.05M NaOH, respectively. In comparison, the spectrofluorometric method demonstrated significantly lower LOQ values of 0.191 µg/ml, 0.204 µg/ml, 0.198 µg/ml, and 0.171 µg/ml in methanol, water, and 0.05M NaOH at 350 nm and 425 nm, respectively. The LOQ values were also lower in emission spectra than absorption spectra, indicating the method's superior sensitivity. The LOD and LOQ values are low in methanol due to the high
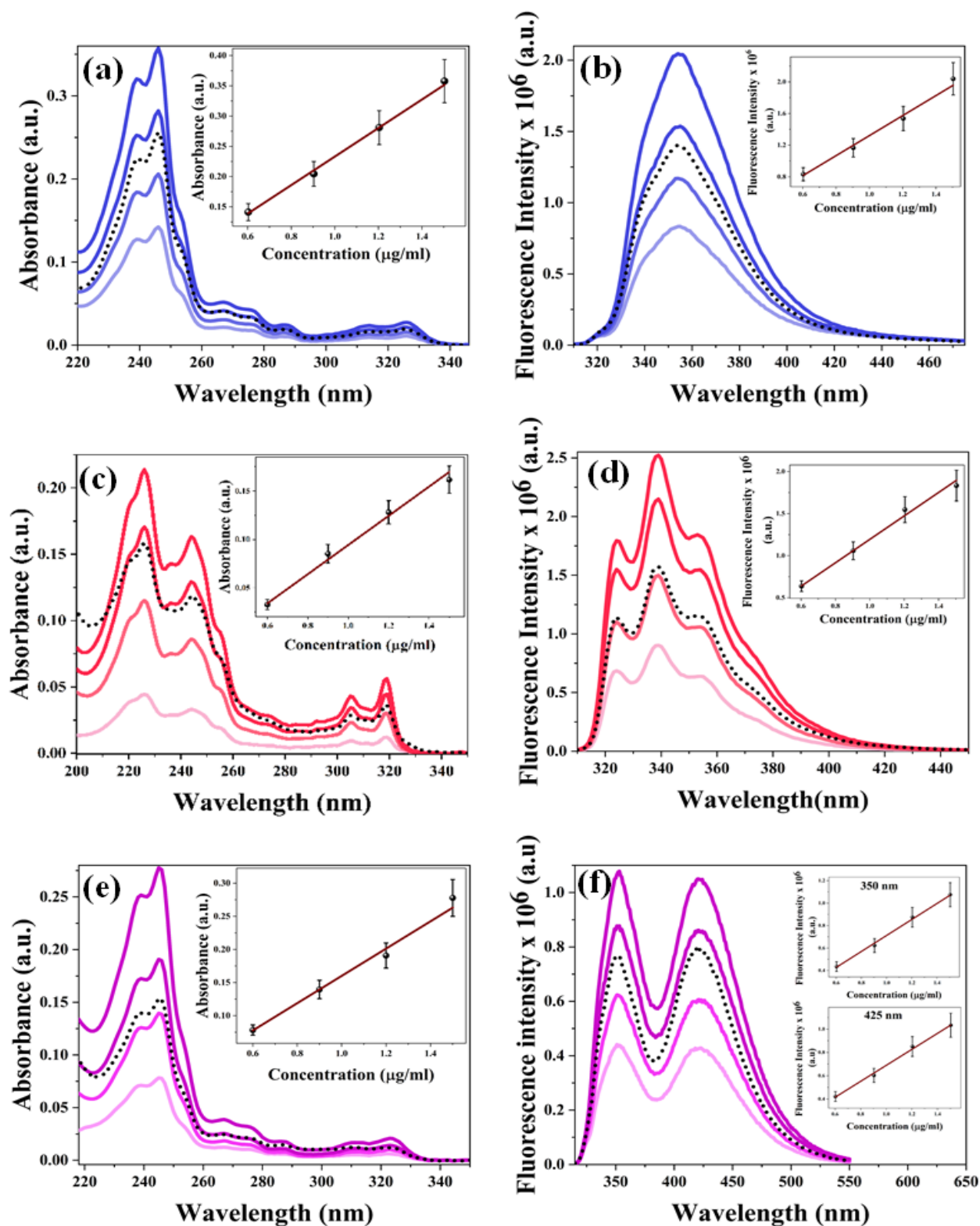
Figure 1. *Absorption spectra of IMQ in (a) methanol, (c) water, and (e) 0.05M NaOH. Emission spectra of IMQ in (b) methanol, (d) water, and (f) 0.05M NaOH. The inset figure shows their corresponding linearity graph (0.60 to 1.60 mg/ml).*

Table 1. Recovery measurements of IMQ from the sachet using absorbance and fluorescence methods.

	Solvent	Slope	Intercept	σ	R²	% Recovery
Absorbance at 245 nm	Methanol	0.236	-0.007	0.0115	0.998	109 ± 5
	Water	0.143	-0.048	0.325	0.990	116 ± 7
	0.05M NaOH	0.216	-0.056	0.0353	0.987	97 ± 10
Emission at 350 nm	Methanol	1.327	-0.005	0.0253	0.990	106 ± 5
	Water	1.357	-0.16	0.0277	0.990	97 ± 7
	0.05M NaOH	0.724	-0.01	0.0144	0.997	107 ± 10
	0.05M NaOH at 425 nm	0.694	-0.004	0.0199	0.998	112 ± 10

σ: Standard deviation of the residuals, R²: Determination coefficient.

Table 2. Limit of detection and limit of quantification values of IMQ using absorbance and fluorescence method

	Solvents	LOD (mg/ml)	LOQ (mg/ml)
Absorbance at 245 nm	Methanol	0.153	0.463
	Water	0.756	2.293
	0.05M NaOH	0.537	1.628
Emission at 350 nm	Methanol	0.063	0.191
	Water	0.067	0.204
	0.05M NaOH	0.065	0.198
	0.05M NaOH at 425 nm	0.056	0.171

LOD: Limit of Detection, LOQ: Limit of Quantification.

solubility of IMQ. Moreover, excipients in the pharmaceutical formulations were not involved in the measurements of IMQ contents, as evidenced by a high agreement between drug levels obtained using different procedures. Comparing the recovery analysis by two spectroscopic methods, one can see no significant difference in the recovery percentage. Either of these methods can be used to analyze the IMQ quantitatively. Conversely, the spectrofluorometric method exhibited lower LOD and LOQ values, underscoring its enhanced sensitivity compared to the spectrophotometer.

Qualitative analysis of IMQ

A time-resolved approach may distinguish several emissive species in a given system, and at the same time, the excited-state properties of molecules can be examined.[20] Time-resolved emission decay profiles of IMQ in standard form and the imiquad cream were collected at 350 nm and 425 nm to understand the excited state dynamics in methanol, water, and the basic solution (**Figure 2**). In methanol, a two-component system with ~2.0 ns having less percentage and a second component with ~4.0 ns at a higher percentage was observed (**Table 3**). The emission decays obtained in water with lifetime components of 1.6 ns and 4.0 ns also match the standard IMQ and the commercial cream. IMQ in 0.05M NaOH exhibits the emission peak at a longer wavelength of 425 nm (**Figure 1f**). The corresponding fluorescence lifetime measurements reveal two-lifetime values; a rising negative amplitude component with a lifetime of 1.9 ns and a decaying component with a lifetime of 8.2 ns (**Table 3**). Lifetime profiles for imiquad

sachet creamand standard IMQ also showed similar lifetime components with a negative component of 1.9 ns and the other is decaying with 8.3 ns. In excited state reactions, this type of negative component is generally called a rising component and isobserved because of ESPT reactions.[18, 23-26]The rising component observed in both the standard formand thecream is due to the anionic species of IMQ formed by excited-stateproton transfer (ESPT) from the amine group present in the quinoline ring to the base.[18] Therefore, the rising component of the IMQ incream matches well with thecomponent of the standard IMQ drug **(Figure 2)**.

The congruence of lifetime components between IMQ in cream and standard form suggests that the pharmaceutical formulation is unaffected by the placebo or stabilizers, which are commonly included to stabilize the drug without introducing any interference.It is a known fact that ESPT is highly sensitive to the surrounding environment; hence, this kind of unique photophysics could be an advantage for performing the quality test of a drug. In this study, IMQ in the creamshows the ESPT, confirming that the drug remains active in sachet. Therefore, we can analyze the quality by monitoring the lifetime studies of the drug molecule. This approach of TCSPC can be further used to detect the active form of the drugs in the quality control department during pharmaceutical formulations.
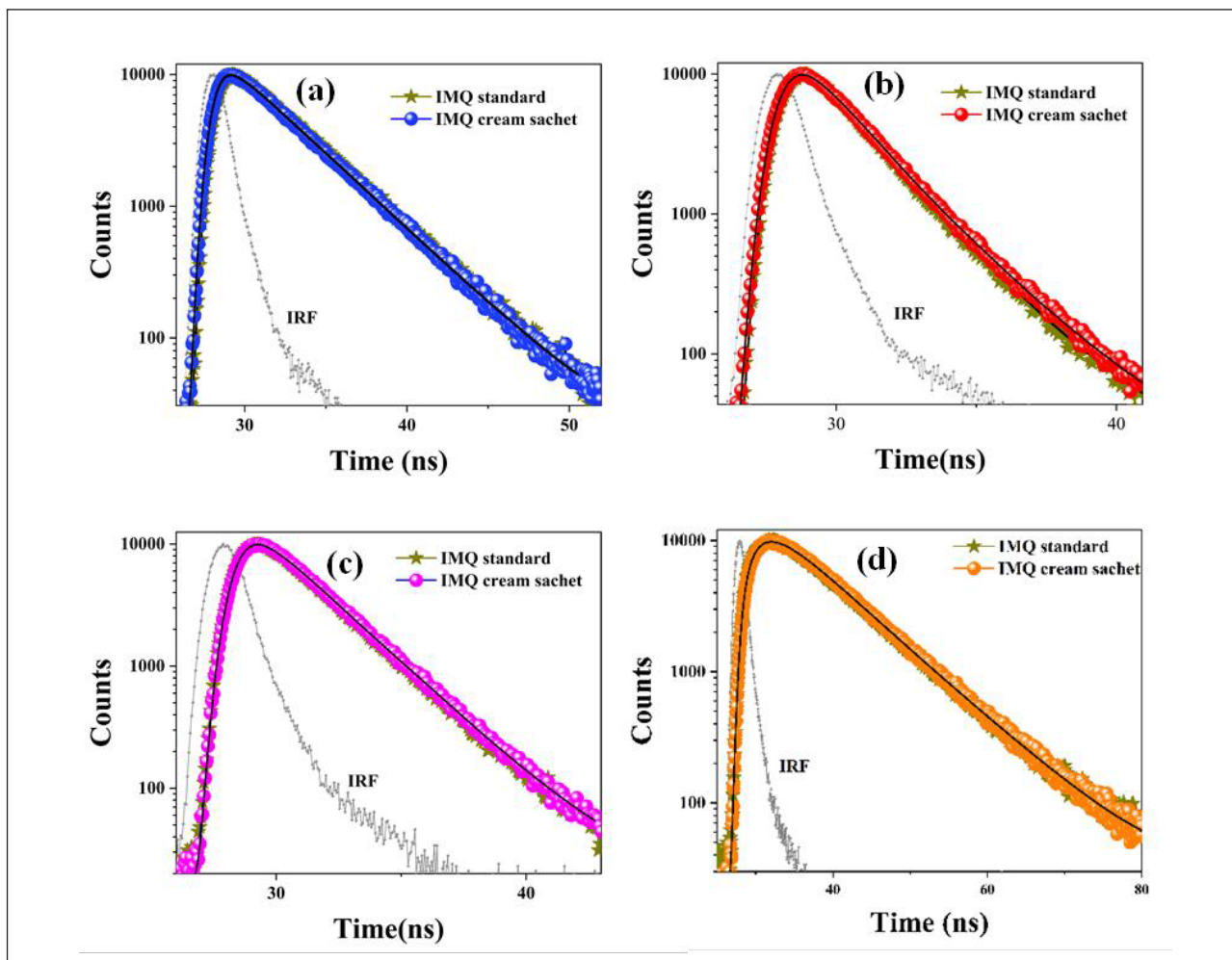

Figure 2: *Time-resolved fluorescence transients of IMQ in (a) methanol at 350 nm, (b) water at 350 nm, (c) 0.05M NaOH at 350 nm, and (d) 0.05M NaOH at 425 nm.Excitation wavelength at 290 nm.*

Table 3. Fluorescence lifetime components of IMQin standard form and incream.

Solvents	λ_{em} (nm)	t_1 (ns)	a_1	t_2 (ns)	a_2	t_{av} (ns)	c^2
Methanol-S*	350	2	0.13	3.9	0.87	3.65	1.1
Methanol-C#	350	2	0.11	3.8	0.89	3.6	1.1
Water-S*	350	1.6	0.83	4.05	0.17	2.01	1.0
Water-C#	350	1.6	0.80	4.0	0.20	2.08	1.0
0.05M NaOH-S*	350	1.73	0.65	2.59	0.35	1.95	1.2
	425	1.93	-0.27	8.16	1.27	5.27	1.1
0.05M NaOH-C#	350	1.74	0.80	3.04	0.20	1.91	1.1
	425	1.90	-0.25	8.26	1.25	5.31	1.0

S*: IMQ standard form, C#: Imiquad cream sachet form

Conclusions

We havedetermined the qualitative and quantitative analysis of the IMQ inimiquad cream.Recovery experiments have shown that the suggested procedures are accurate, with a high percentage of drug recovered (80-120 percent).[22]The recovery studies showed some variation between the spectrofluorometricand spectrophotometric methods, but all results were within the permissible range. The spectrofluorometric method exhibited a greater sensitivity than the spectrophotometric method for quantitative analysis, as evidenced by both LOD and LOQ values. To the best of our knowledge, this is the first qualitative analysis of IMQ using the TCSPC technique. The fluorescence lifetime values of IMQ in imiquad sachet perfectly align with those of standard IMQ across all selected media. A rising component of lifetime values, attributed to ESPT processes, was observed in both the standard IMQ and imiquad cream, confirming the presence of the active form of IMQ in the formulation. This study reveals the effective use of fluorescence lifetime measurements for evaluating drug quality, offering a robust spectroscopic approach to simplify the quantitative and qualitative analysis of other commercial drugs.

References:

1. G. Shinde, R. Godage, R. Jadhav, B. Manoj and B. Aniket, *J. Sci. Technol.*, 2020, **12**, 47-51.
2. R. Bonfilio, M. B. De Araujo and H. R. N. Salgado, *WSEAS Trans. Biol. Biomed*, 2010, **7**, 316-338.
3. F. Sanchez Rojas and C. Bosch Ojeda, *Anal. Chim. Acta*, 2009, **635**, 22-44.
4. A. Bose, I. Thomas and E. Abraham, *Int. J. Adv. Pharm. Res*. 2018, **8**, 01-08.
5. S. El-Ashry, D. El-Wasseef, D. El-Sherbiny and Y. Salem, *Luminescence*, 2015, **30**, 891-897.
6. K. M. Elokely, M. A. Eldawy, M. A. Elkersh and T. F. El-Moselhy, *Int. J. Anal. Chem*, 2011, **2011**.
7. A. Walter, M. Schafer, V. Cecconi, C. Matter, M. Urosevic-Maiwald, B. Belloni, N. Schonewolf, R. Dummer, W. Bloch, S. Werner, H. D. Beer, A. Knuth and M. van den Broek, *Nat Commun*, 2013, **4**, 1560.
8. G. Vishvnath and U. Jain, *Int J Pharm Sci Res (IJPSR)*, 2011, **2**, 58-61.
9. U. Wieland, N. H. Brockmeyer, S. J. Weissenborn, B. Hochdorfer, M. Stücker, J. Swoboda, P. Altmeyer, H. Pfister and A. Kreuter, *Arch. Dermatol.*, 2006, **142**, 1438-1444.
10. M. P. Schön, M. Schön and K.-N. Klotz, *J. Invest. Dermatol.*, 2006, **126**, 1338-1347.
11. E. Hanna, R. Abadi and O. Abbas, *Int. J. Dermatol*, 2016, **55**, 831-844.

12. A. Torres, L. Storey, M. Anders, R. L. Miller, B. J. Bulbulian, J. Jin, S. Raghavan, J. Lee, H. B. Slade and W. Birmachu, *J Transl Med*, 2007, **5**, 7.

13. R. Marks, K. Gebauer, S. Shumack, M. Amies, J. Bryden, T. L. Fox, M. L. Owens and G. Australasian Multicentre Trial, *J Am Acad Dermatol*, 2001, **44**, 807-813.

14. K. R. Beutner, S. L. Spruance, A. J. Hougham, T. L. Fox, M. L. Owens and J. M. Douglas Jr, *JAAD*, 1998, **38**, 230-239.

15. I. H. Wolf, J. Smolle, B. Binder, L. Cerroni, E. Richtig and H. Kerl, *Arch. Dermatol.*, 2003, **139**, 273-276.

16. M. Stanley, *Clin. Exp. Dermatol .* 2002, **27**, 571-577.

17. D. Takkella, L. Martinez-Fernandez and K. Gavvala, *J. Photochem. Photobiol. A: Chem.*, 2024, **457**, 115928.

18. D. Takkella, S. Sharma, L. Martinez-Fernandez and K. Gavvala, *J. Photochem. Photobiol. A: Chem.*, 2022, **431**, 113998.

19. D. Takkella, S. Sharma, J. Vishwakarma, J. Cerezo, L. Martinez-Fernandez and K. Gavvala, *J. Photochem. Photobiol. A: Chem.*, 2024, **447**, 115190.

20. J. R. Lakowicz, *Principles of fluorescence spectroscopy*, Springer2006.

21. A. Shrivastava and V. B. Gupta, *Chron. Young Sci*, 2011, **2**, 21-25.

22. I. H. T. Guideline, *Q2 (R1)*, 2005, **1**, 05.

23. K. Gavvala, R. K. Koninti, A. Sengupta and P. Hazra, *PCCP*, 2014, **16**, 14953-14960.

24. K. Gavvala, N. P. Barthes, D. Bonhomme, A. S. Dabert-Gay, D. Debayle, B. Y. Michel, A. Burger and Y. Mély, *RSC advances*, 2016, **6**, 87142-87146.

25. M. R. di Nunzio, B. Cohen and A. Douhal, *J. Phys. Chem. A.*, 2011, **115**, 5094-5104.

26. Y. Erez and D. Huppert, *J. Phys. Chem. A.*, 2010, **114**, 8075-8082.

	Mr. Takkella Dineshbabu *received his M.Sc. in Physical Chemistry from Andhra University. Currently, he is pursuing his doctoral studies under the guidance of Dr. Krishna Gavvala at the Indian Institute of Technology, Hyderabad. His current research focuses on unravelling the structure and dynamics of DNA in biomimetic media using spectroscopic techniques.*
	Dr. Krishna Gavvala *completed his PhD from IISER Pune under the supervision of Prof Partha Hazra. Soon after completing his two postdoctoral stints, one at University of Strasbourg (France) and other at Leiden University (Netherlands), Dr Krishna joined IIT Hyderabad in 2019 as an assistant professor in chemistry. He is the principal investigator of the Laboratory of Biophysical Chemistry and Spectroscopy. Main objectives of his research group focuses onto investigate chemical and biological macromolecules/systems using spectroscopic, microscopic and computational methods.*

Structural Control of Ultrafast Conformational Dynamics of Fluorogenic Probes: Implication in Sensing Efficacy

Rajib Ghosh[1,2*]

[1]*Radiation and Photochemistry Division, Bhabha Atomic Research Centre, Mumbai 400085,*
[2]*Homi Bhabha National Institute, Anushakti Nagar, Mumbai 400094*
Email: rajib@barc.gov.in

Abstract

Conformational motion in the excited state of fluorophores critically governs photophysical properties and find various applications in sensing and imaging of microscopic viscosity of complex chemical and biological media. Development of viscosity sensitive ultrafast molecular rotor (UMR) probes relies upon the understanding of the excited state dynamics and their implications to viscosity dependent fluorescence signaling. Thus, unraveling controlling parameters of photoinduced molecular motion in UMR is essential for optimization of rotor efficiency. In this article, we summarize the photoinduced charge transfer mediated ultrafast conformational relaxation dynamics in a series of donor-acceptor (D-A) based molecular systems to decipher the role of charge transfer and ground state conformation on ultrafast torsional relaxation dynamics. Our systematic studies revealed that by varying the donor-acceptor strength and conjugation length ultrafast relaxation dynamics of D-A based fluorophores can be fine tuned. Similarly, in a given D-A system, ground state conformation crucially decide speed of conformational motion in excited state which conspicuously correlate to viscosity sensing efficiency. Exquisite sensitivity of ultrafast excited motion on extent of charge transfer and molecular conformation also led us to induce and control ultrafast molecular motion by selective protonation of acceptor site of a bichromophoric UMR. Based on the experimental findings, we summarize the current understanding of excited state conformational dynamics of UMR probes and their relevance toward development of fluorogenic biosensors.

1. Introduction

Conformational relaxation in excited electronic states of organic dyes governs photophysical properties and plays crucial role in molecular sensing and various optoelectronic application.[1-5] Real time capturing of dynamical events associated to geometrical relaxation in photoinduced excited state of organic light absorbing chromophores provides molecular level insight on structure-property relation in chemical dynamics. Photoinduced large amplitude conformational relaxation in molecular excited state is popularly termed as ultrafast molecular rotor (UMR) and provides important information about rigidity and microscopic viscosity by virtue of their viscosity dependence fluorescence signaling. Ultrafast torsion around a single or double bond introduces efficient nonradiative deactivation in nonviscous medium resulting weak emission. Depending on the rigidity offered by the surrounding environment, nonradiative torsional motion gets proportionately restricted, rendering fluorescence intensity enhancement and lifetime lengthening. Thus mapping fluorescence intensity and lifetime of a molecular rotor provides direct information about the rigidity of heterogeneous chemical, biological and biomimetic environments. The excellent fluorescence sensitivity of the molecular rotor is due to occurrence of ultrafast nonradiative torsion induced emission quenching in nonviscous medium and different degree of inhibition of the nonradiative process depending on surrounding viscosity.[4,5] To develop an

efficient viscosity sensor, it is necessary to underpin the influencing factors which govern torsional speed of a molecular rotor.

The ability to control the nonradiative torsional relaxation rate in a molecular system in a desired manner is the key to optimize the sensor efficiency. A priori assessment of the factors governing the rate of torsional motion is a prerequisite and tailoring the molecular rotor property is critical to develop efficient fluorescence sensor and imaging agents for complex chemical fluids, bio-macromolecules and cells. A molecular level understanding of how the torsional relaxation depends on the ground state conformation and finding a structure function relationship of excited state torsional relaxation is desirable to develop better sensors based on UMR principle. In essence, unraveling factors governing molecular motion in excited state is of great significance for fundamental photoinduced chemical dynamics and applied aspects of light driven molecular devices.

In this article, we summarize our recent understanding on how molecular parameters can be favorably tuned to optimize UMR property. We show that the molecular rotor property can systematically be tuned by varying the donor-acceptor strength and by controlling the torsional angle between the two rotating segments of the molecular rotor.[6-11] These two parameters crucially decide the shape of excited state PES on which excited state conformation evolves and consequently govern UMR efficiency.

2. Results and Discussion

2.1 Effect of donor acceptor conjugation on torsional dynamics:

Significant effect of conjugation length between the electron donor and acceptor groups in intramolecular charge transfer (ICT) dynamics has been demonstrated by comparing the photophysical properties of two isomeric N,N-dimethylaminochalcone derivatives (namely, Chalcone-A and Chalcone-B) (Figure 1).[6] In case of Chalcone-B, the distance between the donor (N,N-dimethylaniline) and the acceptor (carbonyl) groups is larger by one ethylene unit as compared to Chalocne-A. The excited singlet (S_1) states of both the isomers have strong ICT character but their photophysical properties are remarkably different. In polar solvents, fluorescence quantum yields of chalcone-A are more than two orders of magnitude lower than those of Chalcone-B. Similarly lifetimes of the S_1 state of Chalcone-A is much shorter (only a few picoseconds) as compared to long lived chaclone-B excited state (several nanoseconds, Figure 1a,b). Remarkable differences in the photophysical properties of these two isomers arise due to occurrence of the ultrafast twisting of the N,N-dimethylaniline (DMA) group (or the TICT process) during the course of deactivation of the S_1 state of the Chalcone-A molecule which has been clearly characterized by ultrafast transient absorption spectroscopic studies(Figure 1c,d). Femtosecond transient absorption experiment revealed that in polar solvents, chalconeA undergoes ultrafast torsion of dimethylaniline unit within 1-2 ps timescale to a nonemissive twisted state followed by internal conversion to ground state within 10 ps. In case of Chalcone-B, nonradiative torsional relaxation is not registered in ultrafast transient absorption experiment (data not shown) which is attributed to larger energy barrier along the twisting coordinate(s). Torsional relaxation in Chalcone-B is not feasible due to stabilization of planar ICT state which makes it emissive and long lived. Large differences in the photophysical properties of the S_1 states of these two molecules is attributed to differences in coupling strength between the donor and acceptor groups. In DMAC-A molecule, this coupling is relatively stronger because of shorter distance between these groups. TDDFT calculations of S_1 state potential energy scan along donor acceptor torsion supports experimental observation showing barrierless PES in case of Chalcone-A as compared to significant barrier for Chalcone-B. Bond responsible for trosional dynamics of Chalcone-A was experimentally conformed by comparing photophysics with a structurally locked molecular analogue.[7]
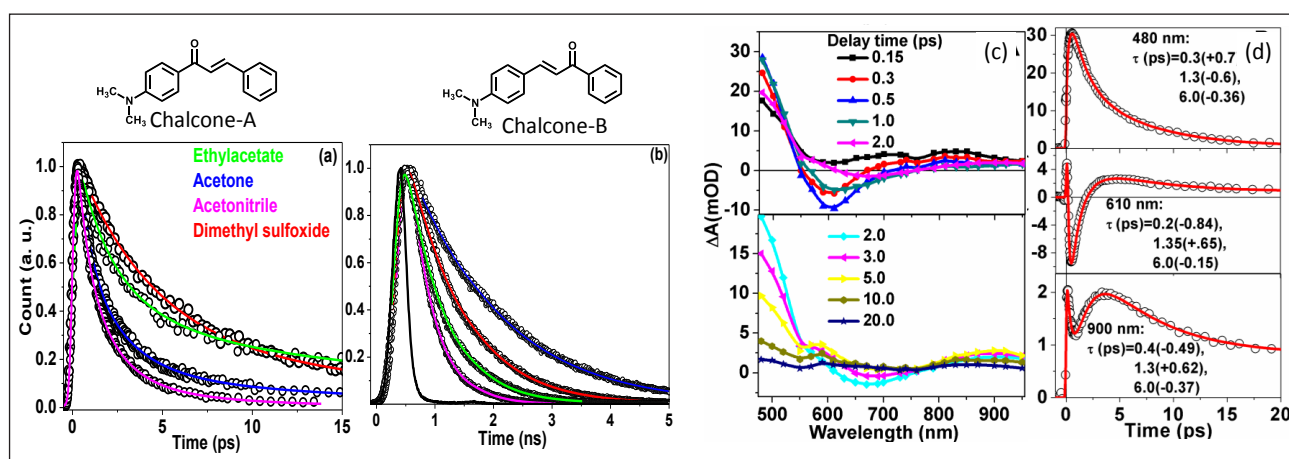
Figure 1: Transient fluorescence decay kinetics of (a)Chalocne-A and (b)Chalcone-B and (c,d) ultrafast transient spectral dynamics of Chalcone-A in acetonitrile. Adapted from ref. 6 (Copyright ACS publication)
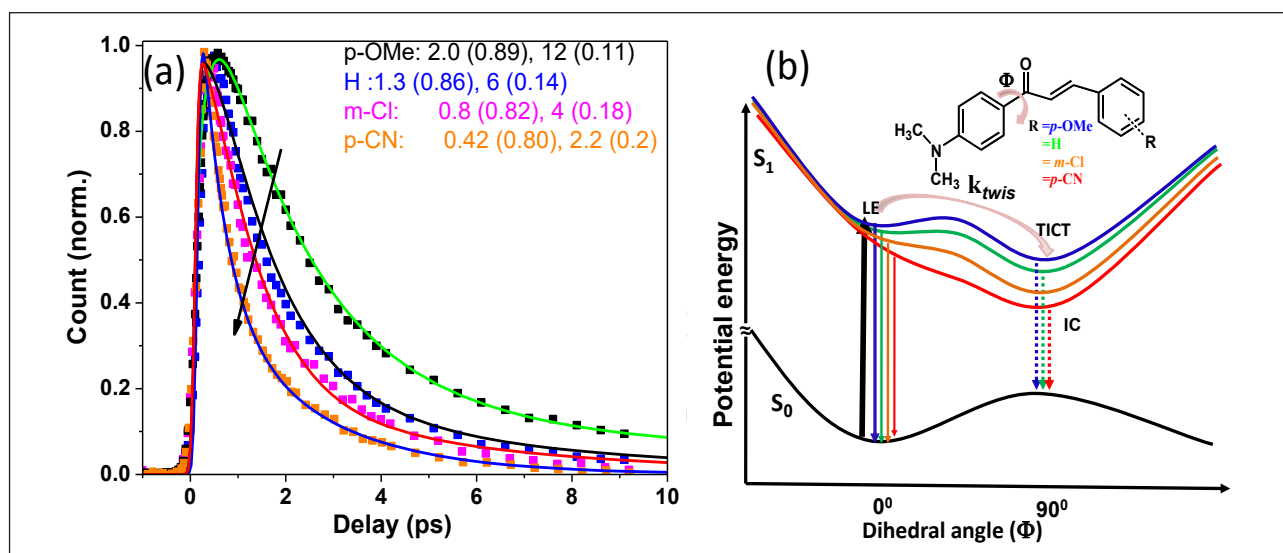

Figure 2. *(A) Ultrafast* **t***ransient emission decay traces of Chalcone-A derivatives in acetonitrile measured by fluorescence-upconversion (λ_{ex} = 390 nm, λ_{em} = 600 nm). Time constants in picosecond and relative amplitudes (in bracket) are also shown in the inset. (b) Schematic potential energy curve of the S_1 surfaceas a function of torsion angle (Φ) around the single bond connecting dimethylaniline and carbonyl groups. Barrier along the TICT coordinate in the S_1 surface decreases with increase in the acceptor strength leading to increase in the twisting rate. Adapted from ref. 8 (Copyright RSC publication)*

2.2. Controlling ultrafast torsional rate by varying acceptor strength: Case of Dimethylaminochalcone derivatives with different acceptor group:

As described in preceding section, facilitated by short conjugation, strong electronic coupling between donor and acceptor units is essential for imparting ultrafast torsional motion in charge transfer fluorophore. To further control the ultrafast molecular motion, one can fine tune the relative strength of the donor and acceptor groups which can modulate intramolecular charge transfer character of the excited state modifying the shape of the potential energy surface. To demonstrate the role of acceptor strength on the ultrafast twisting relaxation dynamics, we synthesized a series of Chalcone-A derivatives with various functional groups attached to the acceptor site (Figure2).[8] Employing femtosecond resolved transient absorption and fluorescence

experiments, twisted intramolecular charge transfer (TICT) relaxation rate of the Chaclone-A derivatives is shown to vary from 2.1 picosecond in weak electron accepting system to about 400 femtosecond in strong electron accepting system (Figure 2a). Increase in acceptor strength, empirically expressed as Hammett's constant, is shown to linearly increase TICT relaxation rate. Based on the experimental results, we propose that variation in charge pulling capacity of the acceptor modifies the torsional barrier along the TICT coordinate in the S_1 state, leading to tunable TICT relaxation rate (Figure 2b). Increase in acceptor strength systematically modulates the TICT coordinate from weak barrier crossing to completely barrierless resulting in acceleration of ultrafast twisting relaxation rate.[8] Systematic tuning of TICT relaxation by varying acceptor strength shown in the present study may be of fundamental importance to design molecules with ultrafast photoinduced charge separation for photovoltaic applications.

2.3 Conformational Control of Ultrafast Molecular Rotor Property: Tuning Viscosity Sensing Efficiency by Twist Angle Variation

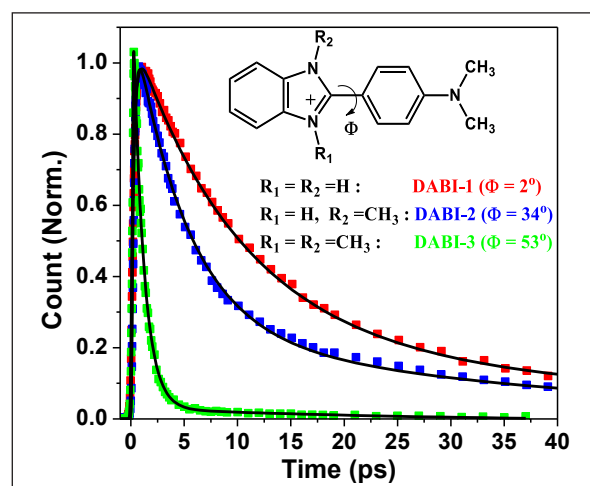Synthesis, photophysics and ultrafast spectroscopic experiments in conjunction

Figure 3: *Transient emission decay kinetics of three DABIs in acetonitrile measured by fluorescence up-conversion method. λ_{ex} = 390 nm, λ_{probe} = 430 nm. Solid line is the fit to the experimental data convoluted with instrument response function. Inset shows the structure of the molecules. Adapted from ref. 9 (Copyright ACS publication)*
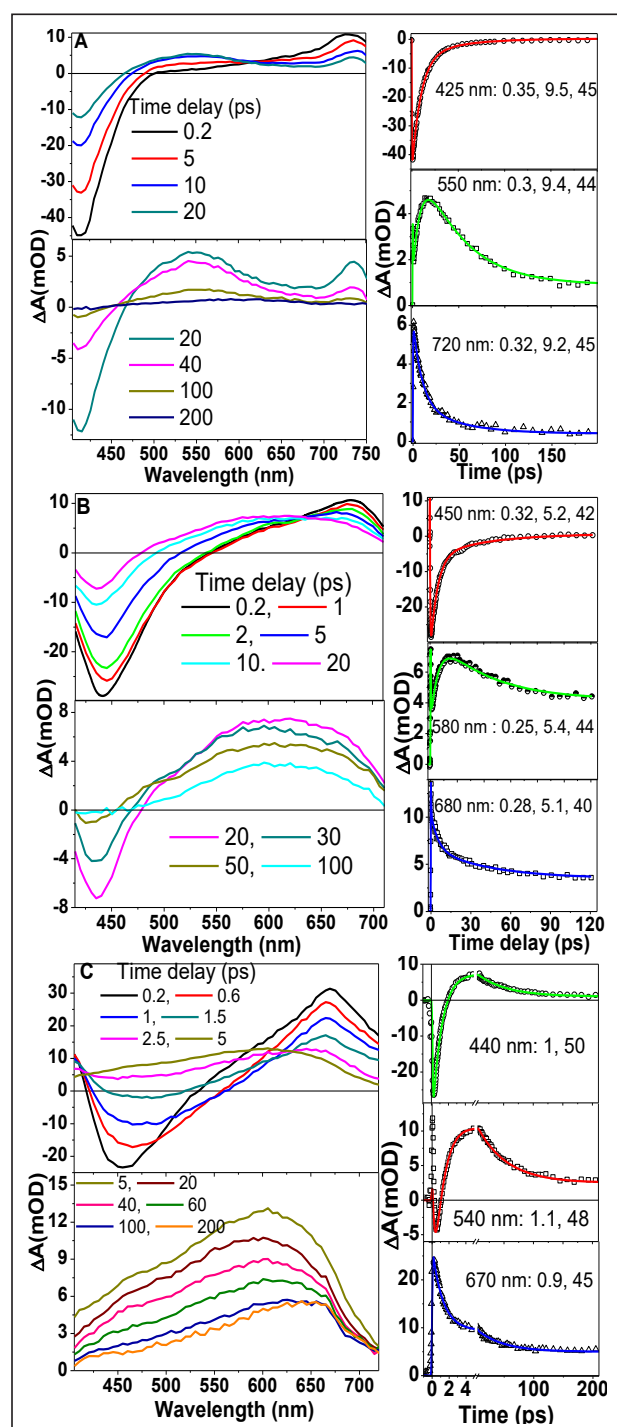
Figure 4. *Transient absorption spectral evolution of DABI 1 (A), DABI-2 (B) and DABI-3 (C) in acetonitrile following femtosecond laser excitation at 390 nm. Right panels show the temporal kinetics (dots) of the transients with sum of exponential fit function (solid line) convoluted with the instrument response function. The time constants (in picosecond) obtained from exponential fit are given in the inset. Reproduced from ref. 9 (Copyright ACS publication)*

with quantum chemical calculation of a series of UMRs based on dimethylaniline donor and benzimidazolium acceptor (DABI) with predefined ground state torsion angle were carried out which led us to unravel influence of ground state equilibrium conformation on ultrafast twisting dynamics of the UMRs and consequent viscosity sensing efficiency.[9] By leveraging the steric influence of hydrogen versus methyl groups, ground state conformation of the three DABIs were varied from near planar (DABI1, 2°) to highly twisted one ((DABI3, 53°). Ultrafast transient emission measurement shows that excited state relaxation gets faster as we move from planar to twisted derivative (Figure 3).

Femtosecond resolved transient absorption measurement showed that for all DABI derivatives, the excited state evolution takes place via the twisted conformation.[9] However, the rate of twisting time systematically increases from DABI1 to DABI3 (**Figure 4**). Viscosity dependent fluorescence lifetime measurement confirmed the molecular rotor behavior of the three systems and Conformation-controlled UMR efficiency has been shown to exhibit commensurate fluorescence enhancement upon DNA binding (Figure5). In essence, ultrafast torsional dynamics around the bond connecting donor and acceptor groups is shown to profoundly influence the molecular rotor efficiency.[9]

2.4. Protonation induced ultrafast torsional dynamics in 9-anthrylbenzimidazole : An acitvatable molecular rotor by protonation:

As described in previous three sections, a systmatic approach led us to understand that short conjugation, strong acceptor strength and pretwisted cnformation in ground state
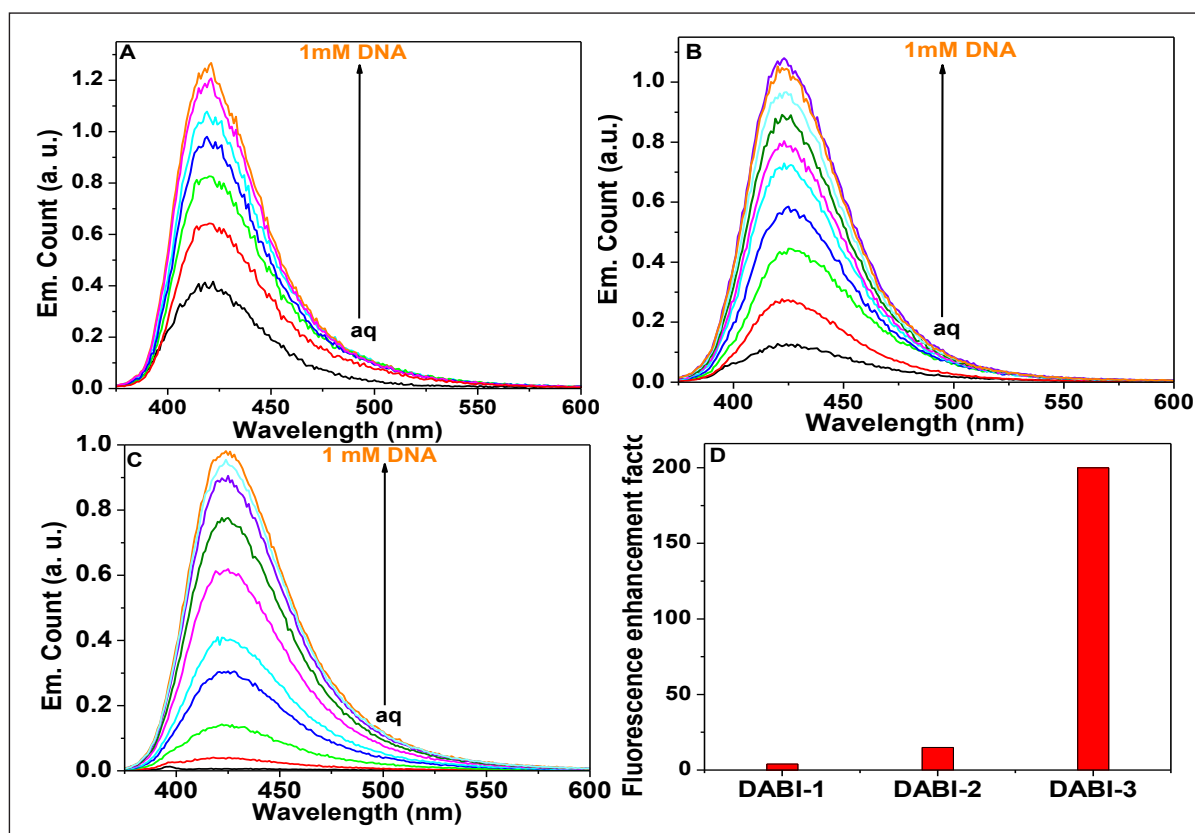

Figure 5. *Change in fluorescence intensity of DABIs upon addition of upto 1 mM calf thymus DNA in aqueous solution. (A) DABI-1, (B) DABI-2 and (C) DABI-3. Experiments were performed at pH 4.5 (D) Comparison of fluorescence enhancement factor (FEF) of three DABIs upon DNA binding. Reproduced from ref. 9 (Copyright ACS publication)*
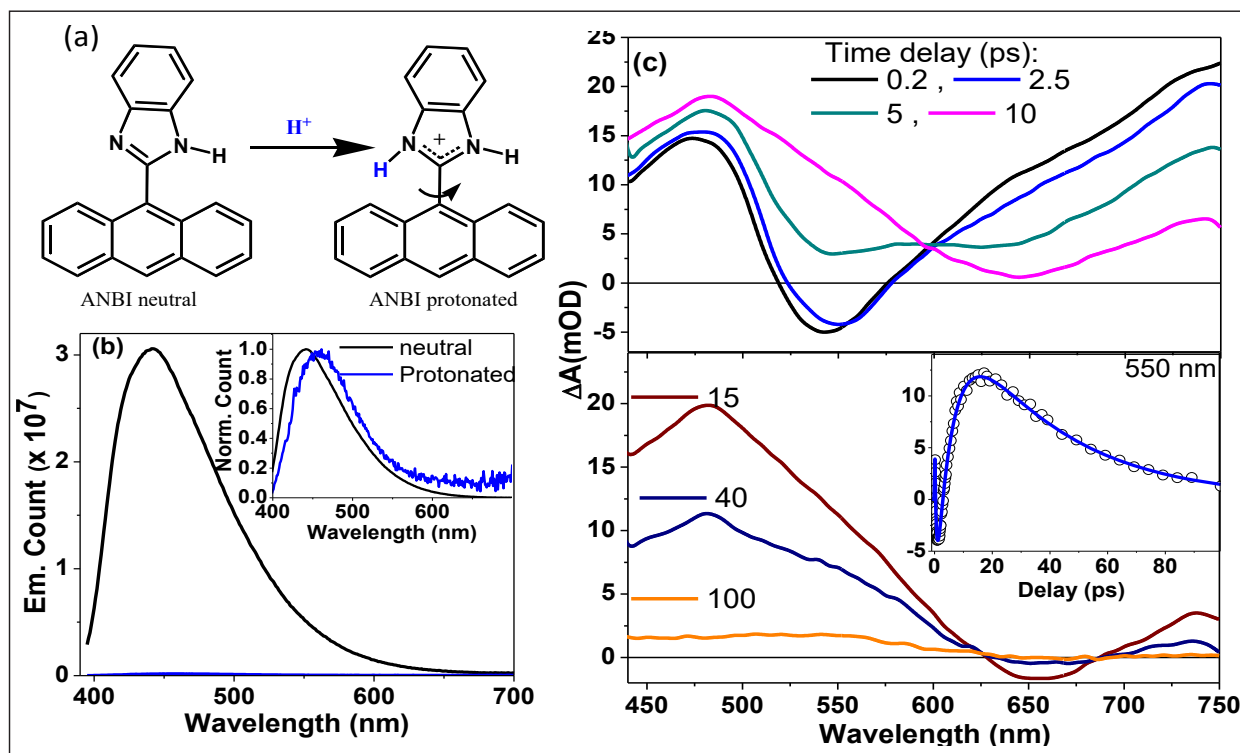
Figure 6: (a) Chemical structure and (b) fluorescence spectra of neutral and protonated ANBI, (c) Transient spectral dynamics of protonated ANBI. Reproduced from ref. 10 (Copyright ACS publication)

helps photoinduced molecuar rotor properties. With these favourable parameters in mind, we set out to explore if we can induce molecular rotor properiy in a given molecular system. In this direction, we designed a bichromophoric molecular system consisting of anthracene and benzimidazole (ANBI, Figure 6a). Weak electron accepting properties of benzimidazole does not alter photophysical properis of anthracene in neutral state. However, protonable site available in benzimidazole (BI) makes it anemable to easy protonation which leads to enhanced charge transfer charcter in the system. As shown in figure 6a and b, protonation led to remarkable change in photophysical properties of ANBI. Femtosecond transinet absorption measurement displayed in figure6c, shows that S_1 state of protonated ANBI deactivates through a twisted intermediate populated with a lifetime of ~6 ps, followed by internal conversion to ground state with a lifetime of ~20 ps. This is in sharp contrast to highly emissive and long lived excited state of neutral ANBI.[10]

In commensurate with the ultrafast results, emission behaviour of protonated ANBI in methanol-glycerol mixture shows high sensitivity to solvent viscosity (Figure 7). Both emission intensity and emission lifetime of protonated ANBI shows systematic increase with solvent viscosity. Log-log plot of emission intensity or emission lifetime exhibit linear correlation in large viscosity range. In contrast, emission properties of neutral ANBI is completely insensitive to solvent viscosity. Thus, protonation induced torsional dynamics is shown to selectively activate moleuclar rotor behaviour in ANBI which can be used as pH activated viscosity sensor.

2.5. Dynamic Planarization Driven Delocalization and Protonation Induced Twisting Dynamics in Anthryl-9-benzothiazole:

When compared to structure of Anthryl-9-benzimidazole (ANBI) described in previous section, Benzothiazole derivative of anthracene (namely ANBT) is more twisted as compared
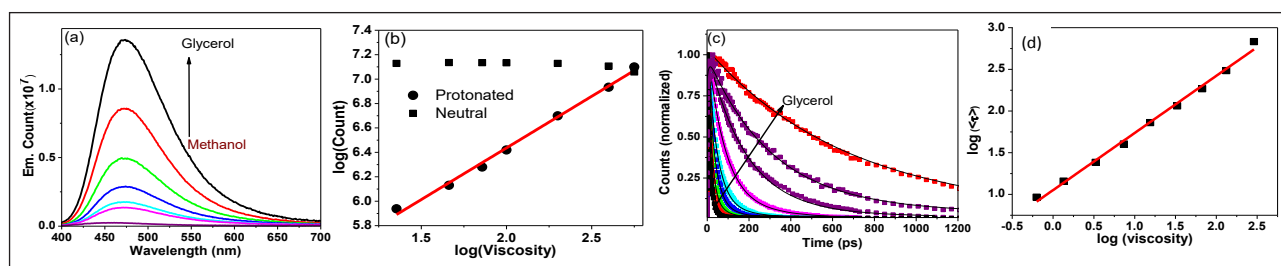
Figure 7. *Viscosity dependent fluorescence intensity (a) and lifetime (c) of protonated ANBI as measured in methanol-glycrol mixture. (c,d) Linear log-log correlation of fluorescence intensity and lifetime wqith viscosity shows excellent molecular rotor behaviour of protonated ANBI, Note, fluorescence of neutral ANBI is insensitive to solvent viscosity. Reproduced from ref. 10 (Copyright ACS publication)*
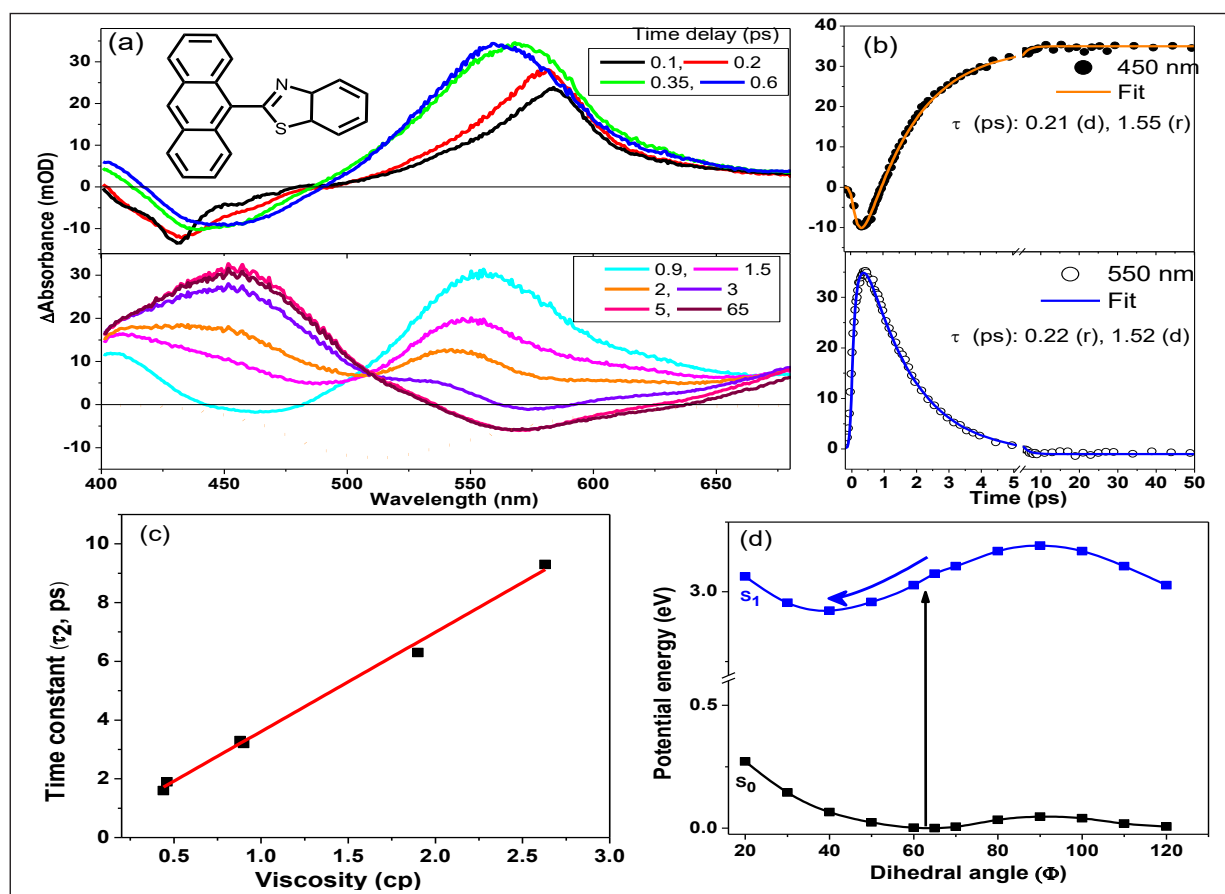

Figure 8: *(a)Transient spectral evolution of neutral ANBT in acetonitrile following 390 nm femtosecond laser excitation. (b) Temporal dynamics of transient absorption signal at two selected wavelengths. (c) Viscosity correlation of ultrafast time constant. (d) DFT/TDDFT calculated potential energy curve of neutral ANBT along central single bond. Adapted from ref. 11 (Copyright ACS publication)*

to anthryl and BI units in ANBI, due to greater steric hindrance imparted by bigger sulphur atom.[11] Moreover, greater charge pulling capacity of benzothiazole can induce higher charge transfer in ANBT as compared to ANBI. These two factors together influence excited state dynamics of neutral ANBT. Ultrafast transient absorption of neutral ANBT in acetonitrile shows an ultrafast evolution of excited state absorption and stimulated emission in a few picosecond timescale (Figure8). Stimulated emission and ESA signal at early timescale evolves to a new
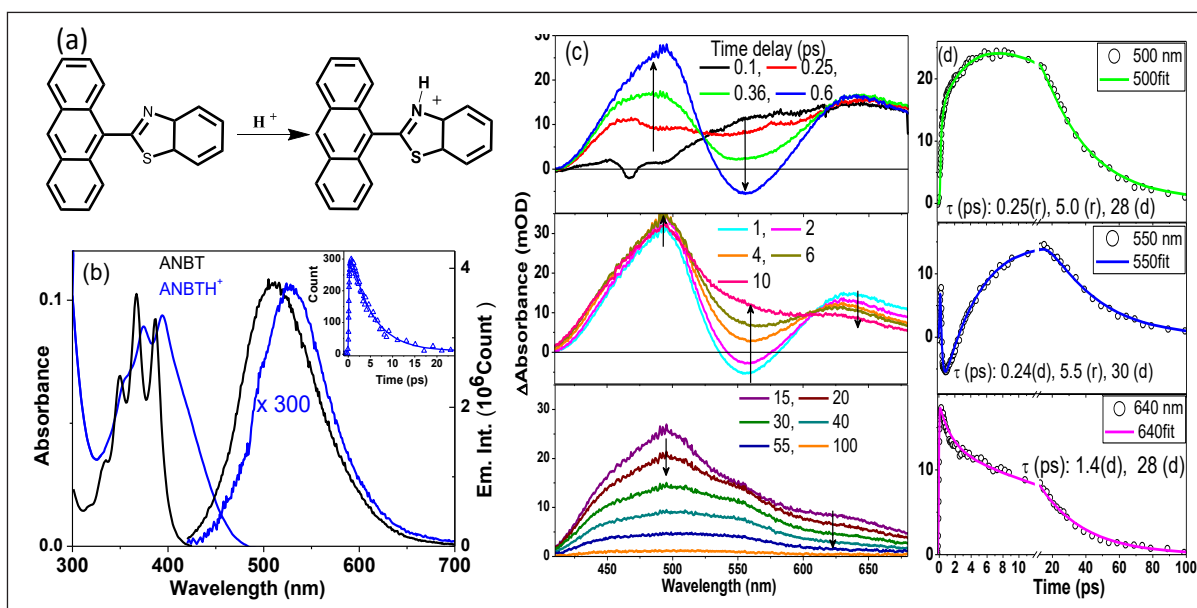
Figure 9:(a)Molecular structure of neutral and protonated ANBT. (b) steady state emission spectra of neutral and protonated ANBT. (c,d)Transient spectral dynamics of protonated AnBT in acetonitrile. Adapted from ref. 11 (Copyright ACS publication)

ESA and long lived stimulated emission. This early time dynamics shows linear correlation with solvent viscosity and thus attributed to conformational relaxation. Quantum chemical calculation revealed that in excited state, AN and BT unit conformationally moves towards more planar configuration to stabilize the S_1 state. Conformational planarization in the excited state of ANBT renders largely Stokes shifted bright emission.

On protonation of the BT unit, low energy charge transfer state is activated, as reflected by a prominent shoulder in absorption spectrum. Protonation remarkably affect the emission strength of the molecule. More than 300 fold quenching occurs due to protonation suggesting ultrafast nonradiative deactivation promoted by protonation (Figure 9a). Transient fluorescence of protonated ANBT reveal lifetime of around 5 ps as compared to 4 ns lifetime of neutral ANBT (Inset of Figure 9b). Femotsecond transient absorption measurement clearly shows that emissive LE state populated within 1 ps timescale gets deactivated to a non-emissive state characterized by strong excited state absorption at 500 nm (Figure 9c). Detailed analysis of transient

absorption data and TDDFT calculation show that ultrafast nonradiative decay of protonated ANBT is associated with twisting relaxation to a perpendicular geometry.[11] Thus, while neutral ANBT undergoes ultrafast planarized motion to a highly emissive excited state, protonation triggers intramolecular charge transfer which facilitate perpendicular twisting of the donor and acceptor group. Spectroscopic behavior of ANBI and ANBT together allowed us to demonstrate that protonation can be utilized to induce torsional motion of D-A based bichromophric fluorophores.

3. Conclusion:

In summary, we show that ultrafast excited state torsional dynamics in D-A fluorophores can be controlled by optimizing electronic and structural parameters. In a given type of donor-acceptor molecules, extended conjugation favours planar emissive state while short conjugation facilitate strong electronic coupling required for twisting induced charge transfer relaxation. Chemically tailored molecular systems with fine tuned acceptor strength can allow timescale of torsional motion to be controlled

in picosecond and femtosecond timescale. As large amplitude torsional motion in excited state is critically dependent of initial Franck-Condon geometry, pre-twisted ground state conformation facilitate faster molecular motion in excited state, enabling more efficient molecular rotor properties. Dimtehylanilino-Benzimidazole derivative (DABI) with pre-defined ground state conformation allowed us to demonstrate correlation of initial twisting with molecular rotor efficiency. Fine tuning of charge transfer and consequent torsional relaxation was exemplified in benzimidazole and benzthizaole derivative of anthracene (ANBI and ANBT) where molecular rotor properties could be triggered by protonation as an external stimulus. In absence of significant intramolecular charge transfer, conformational planarization dynamics in neutral AnBT was shown to be diffusion controlled as revealed from viscosity dependence of picosecond relaxation component. Protonation of BT switches on picosecond nonradiative relaxation to a dark intermediate state by mutual twisting of AN and BT units. Protonation switches the direction of conformational motion from planarization to perpendicular direction. Protonation induced alteration of excited state conformational motion and consequent effect on photophysical parameters is shown to activate viscosity sensing selectively in acidic environment. These results may have further implication in molecular motor and molecular switching applications.

ACKNOWLEDGEMENT

4. References

1. Grabowski, Z. R.; Rotkiewicz, K.; Rettig, W. Structural Changes Accompanying Intramolecular Electron Transfer: Focus on Twisted Intramolecular Charge-Transfer States and Structures.*Chem. Rev.* **2003**, *103*, 3899-4032.

2. Sasaki, S.; Drummen, G. P. C.; Konishi, G. Recent Advances in Twisted Intramolecular Charge Transfer (TICT) Fluorescence and Related Phenomena in Materials Chemistry, *J. Mater. Chem. C*,**2016**, *4*, 2731-2743.

3. Haidekker, M. A.; Theodorakis, E. A., Environment-Sensitive Behavior of Fluorescent Molecular Rotors. *J. Biol. Engin.* **2010**,*4*, 11.

4. Kuimova, M. K.;Yahioglu, G.; Levitt, J. A.; Molecular Rotor Measures Viscosity of Live Cells via Fluorescence Lifetime Imaging. *J. Am. Chem. Soc.***2008**, *130*, 6672–6673.

5. Lee, S. –C.; Heo, J.; Woo, H. C.; Lee, J. –A.; Seo, Y. H.; Lee, C. –L.; Kim, S.; Kwon, O. -P.; Fluorescent Molecular Rotors for Viscosity Sensor, *Chem. Euro. J.* **2018**, *24*, 13706-13718.

6. Ghosh, R.; Palit, D. K.; Effect of Donor–Acceptor Coupling on TICT Dynamics in the Excited States of Two Dimethylamine Substituted Chalcones, *J. Phys. Chem. A*,**2015**, *119*, 11128–11137.

7. Ghosh, R.; Manna, B.; Comparative photophysics and ultrafast dynamics of dimethylaminochalcone and a structurally rigid derivative: experimental identification of TICT coordinate, *Phys. Chem. chem. Phys*. **2017,** 19, 23078-23084.

8. Ghosh, R.; Substituent control of the ultrafast twisted intramolecular charge transfer rate in dimethylaminochalcone derivatives, *Phys. Chem. chem. Phys*. **2018,** 20, 6347-6353.

9. Ghosh, R.; Kushwaha, A.; Das, D.; Conformational Control of Ultrafast Molecular Rotor Property: Tuning Viscosity Sensing Efficiency by Twist Angle Variation, J. *Phys. Chem. B*,**2017**, *12*, 8786-8794.

10. Nandi, A.; Kushwaha, A.; Das, D.; Ghosh, R.; Protonation Induced Ultrafast Torsional Dynamics of Anthrylbenzimidazole : A pH Activated Molecular Rotor, *Phys. Chem. Chem. Phys.*, **2018**, 20, 7014-7020.

11. Ghosh, R.; Nandi, A.; Kushwaha, A.; Das, D.; Ultrafast Conformational Relaxation Dynamics in Anthryl-9-benzothiazole: Dynamic Planarization Driven Delocalization and Protonation-Induced Twisting Dynamics, *J. Phys. Chem. B* **2019**, 123, 5307-5315.

Dr. Rajib Ghosh is a scientific officer at Bhabha Atomic Research Centre, Mumbai, India. After completing M. Sc. in chemistry from University of Burdwan, he joined Bhabha Atomic Research Centre in 2007. He received his Ph. D. degree in 2015 from Homi Bhabha National Institute, Mumbai, for his work on ultrafast structural dynamics in charge transfer molecules in solution. Dr. Ghosh pursued postdoctoral research on ultrafast coherent spectroscopy in Max-Planck Institute for Structure and Dynamics of Matter, Hamburg, Germany. Dr. Ghosh is recipient of University Gold Medal and Homi Bhabha Gold Medal and conferred with young scientist award by the Department of Atomic Energy in 2015and by the National Academy of Sciences, India in 2018. His current research interest includes ultrafast spectroscopy, exciton dynamics and coherent spectroscopy of organic and inorganic materials of optoelectronic interest.

Laser Spectroscopic Investigations of Structure, Stability and Energetics of the Isolated Biorelevant Molecular Complexes

Simran Baweja and Surajit Maity[*]

Department of Chemistry, Indian Institute of Technology Hyderabad, Telangana 502284 India
(Email: surajitmaity@chy.iith.ac.in)

Abstract

In this article, we summarize a novel and robust method developed in our laboratory to probe a reaction by measuring the associated energy barriers of a reaction involving bio molecules and their solvent complexes. The studied systems were the 1:1 complexes of 2,2'-pyridylbenzimidazole (PBI) with H_2O, D_2O, NH_3 and CH_3OH, produced in a supersonic jet and characterized using two-color resonant two-photon ionization (2C-R2PI) technique. The ESPT energy barriers in case of PBI-H_2O and PBI-CH_3OH were measured to be 431±10 cm^{-1} and 410±20 cm^{-1}, respectively, which were further verified using UV-UV hole-burning spectroscopy and kinetic isotopic effect. The isotopic substitution of the tunnelling-proton in PBI-D_2O and PBI-CH_3OD revealed the exact reaction pathway to be a solvent-to-chromophore proton transfer reaction. The energy barriers were measured to be >1000 cm^{-1} in PBI-D_2O and PBI-CH_3OD complex, which were significantly elevated due to the lowering of zero-point energy because of heavy atom insertion in the excited state. This inferred that the solvent-to-chromophore proton tunnelling was found to decrease drastically upon deuterium substitution. The above was further validated by increasing the width of the proton-transfer barrier in PBI-NH_3 complex, which was measured to be >868 cm^{-1}. Herein, the solvent molecule formed a stronger hydrogen bond with the acidic (PBI)N-H group which led to a weaker hydrogen bond interaction between ammonia and the pyridyl-N atom. This subtle change increased the solvent to chromophore proton-transfer barrier. The experimental investigations were further supplemented by computational investigations which provided a conclusive evidence of a novel deactivation pathway in the N-H bearing bio relevant systems.

Keywords: Laser spectroscopy, Gas phase complexes, Energy barriers, Excited state proton transfer, Noncovalent interactions

1. Introduction

The excited-state proton and hydrogen atom transfer are considered as the key reactions associated to the proto-protection and photo-mutation processes in biomolecules.[1-9] Several investigations have revealed that the biomolecules undergo efficient excited-state deactivation through rapid non-radiative decay pathways.[10-13] Over the past two decades, excited-state proton (ESPT) and hydrogen (ESHT) transfer processes have been widely studied in the gas phase molecular complexes using various laser spectroscopic techniques.[14-17] For an efficient excited state hydrogen/proton transfer reaction to occur, the molecule must have a hydrogen/proton donor as well as acceptor groups. The N-H and O-H containing molecules such as azaindoles, 1-naphthol, hydroxyquinolines and phenol have demonstrated increased photo-acidity upon UV excitation. Therefore, such systems were frequently utilized to carry out both energy-resolved and time-resolved excited state investigations.[14,18-21] Previous ESPT and ESHT studies on the gas phase ammonia complexes of phenol and 1-naphthol reported the directional nature of proton transfer. In the reaction, the proton is transferred from the chromophore to the solvent molecule followed by deactivation via internal conversion.[14,18-20,22]

In the current study, we have employed the various micro-solvated complexes of PBI (2,2'-pyridylbenzimidazole) to explore the exact reaction pathways and other crucial factors governing the excited state processes. The PBI molecule is widely known to undergo excited state proton transfer in the aqueous solution.[23,24] The PBI molecule possesses a benzimidazole N-H group connected to a N containing pyridinering via a single C-C bond. The proximity of both the groups makes it a suitable candidate for investigating the excited state processes, utilizing the solvents connected via a cyclic hydrogen bonded network.[25] The molecule exhibits widespread bioactivity due to the presence of a benzimidazole moiety.[26,27] Additionally, it is considered as a potential photocatalyst in water splitting due to the basic nature of pyridine ring.[28] The present study provides compelling evidence of the novel solvent-to-chromophore proton transfer pathway which lead to the deactivation of the excited complex in biomolecules. Overall, the current work offers a fresh and unique perspective on the deactivation mechanisms of photo-excited N-containing biorelevant molecules.

2. Methods

The binary complexes of PBI-H_2O, PBI-D_2O, PBI-CH_3OH, PBI-CH_3OD and PBI-NH_3 were produced using the supersonic jet-cooled conditions in a differentially pumped molecular beam machine. The sample (PBI) was heated to 393 K to obtain a sufficient vapour pressure and was co-expanded with the vapours of H_2O/D_2O/NH_3/CH_3OH/CH_3OD seeded in 2 bar of He in the vacuum. The details of the experimental setup are discussed elsewhere.[29] The complexes were characterised using two-color resonant two-photon ionization (R2PI) and UV-UV hole-burning (HB) spectroscopic techniques. In R2PI technique, the jet-cooled molecular complexes were electronically excited using the frequency-doubled output of a tunable dye laser which was pumped by the second harmonic of an Nd:YAG laser. The 4th harmonic (266 nm) of the same

Nd:YAG laser was used for ionization to avoid any pulse-to-pulse temporal jitter.

To record the hole-burning spectra, a third hole-burning (HB) laser obtained from the second harmonic output of a dye laser pumped by a second Nd:YAG laser, was introduced 200 ns prior to the excitation laser. The HB laser was scanned while the excitation laser was fixed at the $S_1 \leftarrow S_0$ electronic origin of the complex and a dip in the R2PI signal was obtained at each resonant transition due to HB laser, as it depopulates the ground state irrespective of the lifetime of the final excited vibrational state. The HB spectrum can thus measure the vibrational frequencies of the S_1 state irrespective of the lifetime of the higher vibrational levels in the excited state. All the experiments were performed with an ~0.2 mJ perpulse of UV laser power and a beam size of ~2 mm.

The calculations involving the ground and excited-state geometry optimizations were carried out using the dispersion corrected density functional theory (DFT-D4) method with the B3LYP density functional and the polarization functional def2-TZVPP/def2-TZVP basis set. The calculated structures were further verified using subsequent frequency calculations.The initial structures of the PBI-S complexes were generated by placing the respective solvent (S) molecule around PBI such that it formed a hydrogen-bonded wire between the pyridine N and the benzimidazole N-H groups. The proton transfer (PT) state of the PBI-S complex was generated by adding a OH^- (for the PBI-H_2O complex), CH_3O^- (for the PBI-CH_3OH and NH_2^- (for the PBI-NH_3 complex) to the protonated PBI cation ($PBIH^+$), forming a hydrogen-bond between the N-H groups. All the calculations were performed using the TURBOMOLE program.[30]

3 Results and Discussion

3.1 Electronic spectra of PBI-S complexes

Figure 1 depicts the two-color resonant two-photon ionization (R2PI) spectra of PBI (trace (a)), PBI-H_2O (trace (b)), PBI-D_2O (trace (d)), and
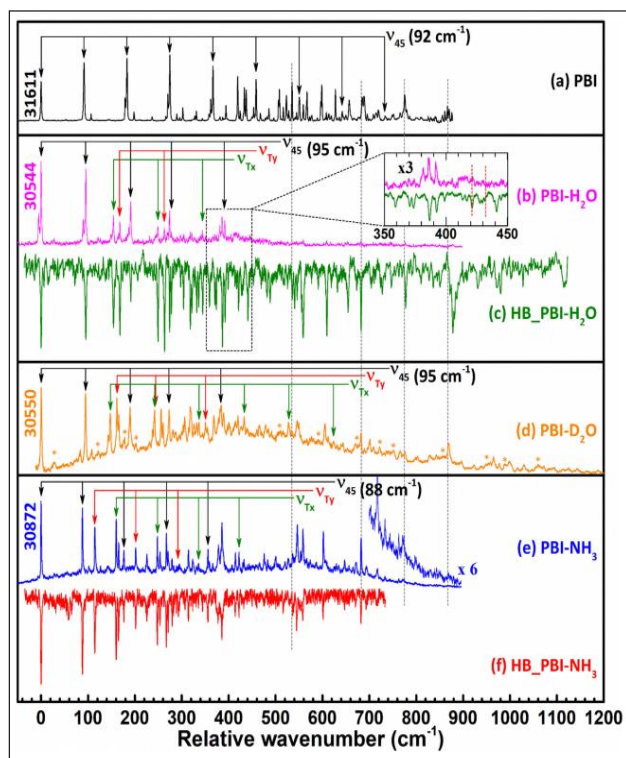
Figure 1.2 *C-R2PI spectra of the $S_1 \leftarrow S_0$ band systems of PBI 0^0_0 (a), PBI-H$_2$O (b), PBI-D$_2$O (d), and PBI-NH$_3$ (e). Trace (c)and(f) represent the hole-burning spectra of the PBI-H$_2$O and PBI-NH$_3$ complexes.*

PBI-NH$_3$ (trace (e)), respectively. The band origins for the $S_1 \leftarrow S_0$ transitions in PBI, PBI-H$_2$O, PBI-D$_2$O, and PBI-NH$_3$ systems are obtained at 30611, 30544, 30550, and 30872 cm-1, respectively.[31,32] which are significantly red-shifted by 1067, 1061, and 739cm^{-1}, respectively, upon complexation. The band origin positions of the PBI-S complexes are highly sensitive to the docking preferences of the admolecules. The substantial red shifts in case of all the solvent complexes suggest the binding of the solvents via hydrogen bonding to the imidazolyl-NH (N$_1$H) group.The high red-shift also implies the greater stabilisation of the electronically excited solvent clusters.The inverted traces in Figure 1(c) and(f) depict the UV-UV hole-burning (HB) spectra of the PBI-H$_2$O and PBI-NH$_3$ complexes, which confirm the presence of a single isomer in the observed spectral range for each system.

3.2 Structures of PBI-S complexes

Figure 2 shows the most stable geometryoptimised structures of the PBI-H$_2$O, PBI-NH$_3$ and PBI-CH$_3$OH complexes, calculated at the B3LYP-D4/def2-TZVPP level of theory. The calculated bond lengths are given in Table 1. In the PBI-H$_2$O structure, the hydrogen bond length of N$_1$H$\cdots$O (1.70 Å) is found to be marginally longer than that of OH$\cdots$N$_P$ (N$_P$ = pyridinyl N) at 1.65 Å. The respective experimental frequency of the intermolecular ν_{Tx} mode (the internal translational motion of H$_2$O along the N$_1$H$\cdots$O hydrogen bond) is obtained at 154 cm^{-1}. The ν_{Ty} mode due to the internal translational motion of H$_2$O along the OH$\cdots$N$_P$ hydrogen bond is positioned at 168 cm^{-1}, which is marginally higher by 14 cm^{-1} compared to the n$_{Tx}$ mode. Both the experimental ν_{Tx} and ν_{Ty} values are in good agreement with the calculated data. Hence, the OH$\cdots$N$_P$ hydrogen bond strength can be considered marginally higher than the N$_1$H$\cdots$O bond. In PBI-D$_2$O, the frequency values of ν_{Tx} and ν_{Ty} modes decreased to 148 and 162cm^{-1}, respectively, due to the higher molecular weight of the solvent molecule. However, the bond strength order remained unaltered upon isotopic substitution.
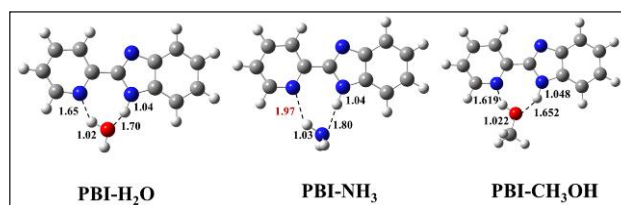

Figure 2. *Geometry optimized structures of PBI-H$_2$O, PBI-NH$_3$ and PBI-CH$_3$OH at B3LYP-D4/def2-TZVPP level of theory.*

In case of most stable structure of PBI-NH$_3$ complex, the N$_1$H$\cdots$N hydrogen bond length (at 1.80 Å) is found to be much shorter than that of the NH$\cdots$N$_P$ bond (at 1.93 Å), suggesting the presence of a weaker NH$\cdots$N$_P$ bond. The experimental intermolecular ν_{Ty} mode due to the internal translation of NH$_3$ mode along the NH$\cdots$N$_P$ bond was found to be significantly lower at 115 cm^{-1} than the ν_{Tx} mode at 160 cm^{-1}.

Table 1. Experimental band-origin transitions 0_0^0 and spectral shifts ($\Delta\nu$ in cm^{-1}) for PBI, PBI-H$_2$O, PBI-NH$_3$, and PBI-CH$_3$OH complexes are given in wavenumbers (cm^{-1}). Hydrogen bond lengths of N$_1$H$\cdots$(N/O) and (O/N)H$\cdots$N$_P$ are also mentioned in Å.

Systems		$\Delta\nu$	N$_1$H $\cdots$N/O	(O/N)H $\cdots$N$_P$
PBI	31611	**0**	-	-
PBI-H$_2$O	30544	**-1067**	**1.70**	**1.65**
PBI-NH$_3$	30872	**-739**	**1.80**	**1.97**
PBI-CH$_3$OH	30400	**-1211**	**1.652**	**1.619**

Additionally, the ν_{Ty} mode is lowered by 53 cm^{-1} compared with that in PBI-H$_2$O, suggesting a weaker hydrogen bond strength of the NH$\cdots$N$_P$ bond. The above experimental observation is in good agreement with the calculated bond length data.[33] Ammonia is known to have a higher gas-phase basicity compared to water due to which it acts as a stronger hydrogen bond acceptor than a donor. Hence, the formation of a stronger N$_1$H$\cdots$N over NH$\cdots$N$_P$ is fully justified. Moreover, the binding energy values in the S$_1$ state of the PBI-H$_2$O and PBI-NH$_3$ complexes are calculated as 63 kJmol^{-1} and 42 kJmol^{-1}, respectively, which suggested the lower stabilisation of the PBI-NH$_3$ complex. The above can be correlated to the lower $\Delta\nu$ values (-739 cm^{-1}) of the NH$_3$ compared to the H$_2$O complex.

In the R2PI spectrum of PBI-CH$_3$OH complex (Figure 3), the ν_{Tx} mode (164 cm^{-1}) corresponds to the internal translational motion of the CH$_3$OH along the N$_1$H$\cdots$O coordinate, which agrees well with the calculated value at 164 cm^{-1}.[34] The ν_{Ty} mode at 185 cm^{-1} represents the internal translational motion along the O-H$\cdots$N$_P$ vibrational mode which correlates well to the calculated mode at 182 cm^{-1}. The higher value of ν_{Ty} than the ν_{Tx} value implies a stronger O-H$\cdots$N$_P$ hydrogen bond than that of N$_1$H$\cdots$O in the complex. The above is in line with the results obtained for PBI-H$_2$O complex.

3.3 Excited-state processes in binary complexes

In the R2PI spectrum of PBI-H$_2$O complex, the bands present within + 500 cm^{-1} are assigned as the low-energy intramolecular modes (ν_{45}, ν_{44}, ν_{43} and combinations of the above modes) and intermolecular modes (the combination of ν_{Tx}/ν_{Ty} with the intramolecular modes ν_{45}). The peaks present in the higher energy region showed a decrease in the intensity and the bands completely disappeared beyond 421 cm^{-1}.

This can be explained using the three possible photophysical and photochemical processes. (i) Franck-Condon factor: A significant difference in the electronic structure of the complex upon electronic excitation can substantially reduce the band intensities in the R2PI spectrum. (b) Quantum tunnelling: In the R2PI experiment, the signal intensit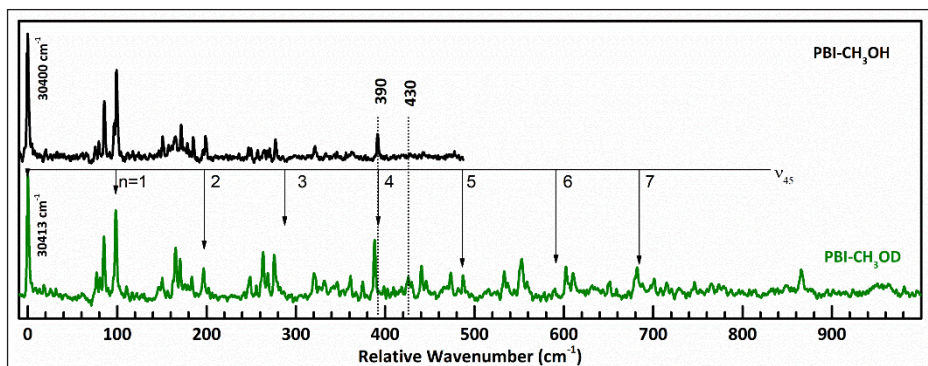y depends on the lifetime of the excited vibrational states. In PBI-H$_2$O, the lifetime of the vibrationless S$_1$ state was measured to be of the same order of magnitude (~5 ns) as the laser pulse width. A short lifetime in the S$_1$ vibrational state (<100 ps) due to enhanced quantum mechanical tunnelling of a hydrogen atom/proton can cause the R2PI

Figure 3. *Two-colour resonant two-photon ionization spectra of the S$_1\leftarrow$S$_0$ transitions of the PBI-CH$_3$OD complex is compared against that of the PBI-CH$_3$OH complex. The vertical arrows represent the progression of ν_{45} modes till n=6.*

signal to disappear. (c) Energy barrier: The disappearance of bands in the R2PI above 0_0^0 + 421 cm^{-1} can also be due to the fast deactivation of the excited state via the proton/ hydrogen atom transfer reaction.

If the molecule is excited to a state higher in energy than the energy barrier of the subsequent reaction process, the above reaction can be efficient. Further, a hole burning (HB) spectrum of the PBI-H$_2$O complex(Figure 1(c)) complex is recorded to understand the effect of the above three processes in the complex. In the HB experiment, the scanning laser introduced prior depletes the population of the vibrationless S_0 state at each Franck-Condon active $S_1 \leftarrow S_0$ transition, independent of the lifetime of the S_1 state. The bands in the HB spectrum are observed till + 1120 cm^{-1}, confirming the Franck-Condon activity on both the intra- and intermolecular vibrational bands in the S_1 state.

Moreover, the intensities of the intramolecular modes in the HB spectrum of PBI-H$_2$O were found to be similar to that in the R2PI spectrum of PBI. This infers that the disappearance of the R2PI signal in the PBI-H$_2$O complex cannot be due to the loss of Franck-Condon activity. However, in the 200-400 cm^{-1} region, the intensities of intermolecular modes in the R2PI spectrum of PBI-H$_2$O are significantly lower compared to the corresponding peaks in the HB spectrum. Since these intermolecular vibrational modes are the internal translational motion of water molecules towards the $N_P(\nu_{Ty})$ and N_1-H (ν_{Tx}) groups, hence, quantum tunnelling of a proton/hydrogen is feasible. Therefore, the above can reduce the peak intensities of the intermolecular modes in the R2PI spectra.

To further verify the scope of tunnelling, we have utilized the kinetic isotope effect employing the PBI-D$_2$O system. The R2PI spectrum of the PBI-D$_2$O complex is shown in Figure 1(d). The isotopic H/D substitution does not alter the ground and excited state geometries and the properties of electronic transitions of a complex. The above is evident from the marginal blue shift

of 6 cm^{-1} for the band with respect to that of the PBI-H$_2$O complex, which is in good agreement with the calculated value of 5 cm^{-1}. However, the high mass of D/D$^+$ can substantially reduce the rate of quantum tunnelling which can lead to an increase in the intensity of the intermolecular bands in the spectrum. In addition, zero-point vibrational energy of an electronic state of a molecule can significantly decrease due to H/D substitution, which can elevate the activation energy of a reaction.

In the R2PI spectrum of PBI-D$_2$O, the bands are observed till 0_0^0 + 1030 cm^{-1}, which implies that the excited state energy barrier can be as high as 1030 cm^{-1}, which is much higher than that of the PBI-H$_2$O complex. The band intensities of the transitions in PBI-D$_2$O are found to be similar to those observed in the HB spectrum of PBI-H$_2$O (Figure 1). Moreover, the intensities of the intramolecular vibrational modes in both H$_2$O and D$_2$O are found to be similar before the cut-off band of 0_0^0 + 421 cm^{-1}. However, the intensities of the intermolecular modes in PBI-D$_2$O above 200 cm^{-1}(Figure 4) are significantly enhanced which can be correlated to the comparatively much slower quantum tunnelling of D/D$^+$ in the PBI-D$_2$O complex. This infers that the lifetimes of the excited vibrational states have increased significantly upon isotopic substitution as the quantum tunnelling rate is reduced. This strengthens the possibility of a favourable quantum mechanical tunnelling in the PBI-H$_2$O complex. Further, to understand the rate of quantum tunnelling in different vibrational modes in the S_1 state of PBI-H$_2$O complex, the ratio of the peak intensities of the R2PI bands of PBI-D$_2$O with that of PBI-H$_2$O as $\frac{I_D}{I_H} = \frac{I_{PBI-D_2O}}{I_{PBI-H_2O}}$ are calculated. The intramolecular bands at 274 and 392 cm^{-1} show $\frac{I_D}{I_H}$ intensity ratios of 1.40 and 1.86, respectively. Similarly, the intermolecular bands in the same region, positioned at 263, 303 and 345 show $\frac{I_D}{I_H}$ values of 3.91, 3.91 and 2.66, respectively. This confirms the presence of strong quantum mechanical tunnelling in the PBI-H$_2$O complex.
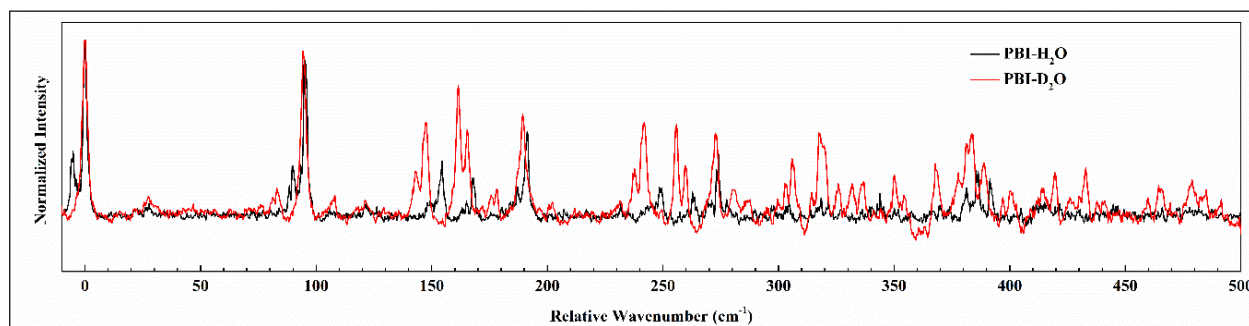
Figure 4. *The baseline corrected normalized R2PI spectra of PBI-H$_2$O and PBI-D$_2$O are shown to compare the kinetic isotope effect on various vibrational modes. The I$_D$/I$_H$ values are given in maintext Table 2 of the article, calculated by integrating each peak.*

Similar to the PBI-H$_2$O system, the excited state mechanisms in case of PBI-CH$_3$OH are also investigated using the R2PI method(Figure 3) and kinetic isotopic effect. The S$_1$←S$_0$ band origin transition 0_0^0 of the complex is observed at 30400 cm^{-1},which is redshifted by 1211 cm^{-1}, compared to the PBI monomer. The large red shift confirms the binding of the methanol molecule to be similar to that of water in the PBI-H$_2$O complex. In PBI-CH$_3$OH complex, the v$_{45}$ mode is obtained at 99 cm^{-1}, with a progression of n = 4. The above shift is similar to that of PBI-H$_2$O complex (95 cm^{-1}) which supports the similar intermolecular structure of both the complexes. The most stable structure of PBI-CH$_3$OH structure showed hydrogen-bonded linkages between PBI and the solvent molecules as OH···N$_P$ and N$_1$H···O, with a bond distance of 1.62 Å and 1.65 Å, respectively, which complies well with the experimental observation.

The R2PI spectrum of the PBI-CH$_3$OD complex(Figure 3) was recorded and the band origin of the complex is observed at 30413 cm^{-1}, which is similar to that of PBI-CH$_3$OH complex. The bands in the 150-390 cm^{-1} region are found to be more intense in PBI-CH$_3$OD complex than the PBI-CH$_3$OH complex. The above can be due to the shorter lifetime of the vibrational states in the PBI-CH$_3$OH complex due to the enhanced quantum mechanical tunneling of the proton/hydrogen atom transfer. However, the tunneling is significantly reduced in the PBI-CH$_3$OD complex due to the increase in mass.

Additionally, the zeropoint vibrational energy of the complex also decreases because of the isotopic substitution. Due to the above factors, the vibrational bands were observed up to +981 cm^{-1} in the R2PI spectrum of PBI-CH$_3$OD complex. The above observations align well with the results obtained for PBI-H$_2$O and PBI-D$_2$O complexes. Therefore, the adjacent strong higher energy intramolecular band at 430 cm^{-1} in PBI-CH$_3$OD must be the first lowest energy missing vibrational mode of the PBI-CH$_3$OH complex. Hence, the band at 430 cm^{-1} is considered as the upper limit of the excited state energy barrier of the PBI-CH$_3$OH complex. Based on the above, the energy barrier is experimentally measured to be 410 ± 20 cm^{-1}.

In the R2PI spectrum of the PBI-NH$_3$complex (given in Figure 1(e)), the bands are observed till + 868 cm^{-1} with high band intensities above 0_0^0 + 421 cm^{-1}, which is very different from the spectrum observed for the PBI-H$_2$O complex. Moreover, the PBI-NH$_3$ structure in the S$_1$ state possess a wider potential along the N$_P$···H$_b$ distance due to which a lower proton/hydrogen tunnelling rate of solvent to N$_P$ and a higher energy can be expected. The above is evident from the R2PI spectrum as well wherein the high band intensities are observed in higher energy region. The recorded HB spectrum also depicts nearly similar depletion patterns as those of the R2PI spectrum till 733 cm^{-1}. Additionally, both the intermolecular bands and the intramolecular modes in the R2PI spectra of NH$_3$ were found

to be equally intense, indicating the negligible quantum tunnelling in the energy region up to + 733 cm^{-1}. The above confirms the higher energy barriers and a much lower quantum mechanical tunnelling for the excited state processes in the PBI-NH$_3$ complex.

4. Conclusions

In this article, we have demonstrated a unique laser spectroscopic approach to probe the energy barriers of excited state processes in PBI and its solvent complexes. The 1:1 solvent complexes of H$_2$O, D$_2$O, NH$_3$ and CH$_3$OH with PBI were produced in a supersonic jet and characterized using two-color resonant two-photon ionization (2C-R2PI) technique. The ESPT energy barriers in case of PBI-H$_2$O and PBI-CH$_3$OH were measured to be 431±10 and 410±20 cm^{-1} respectively. The lower energy barrier in case of PBI-CH$_3$OH complex compared to that of PBI-H$_2$O is most likely due to the marginally high acidity of methanol in the gas phase than water. Using the kinetic isotopic effect, the exact reaction pathways were found to be a solvent-to-chromophore proton transfer reaction. The excited state barriers were measured to be >1000 cm^{-1} in both PBI-D$_2$O and PBI-CH$_3$OD complexes, which were significantly elevated due to the lowering of zero-point energy because of heavy atom insertion. The above implies that the hydrogen/proton tunnelling was decreased drastically upon deuterium substitution. To further verify this, the width of the hydrogen/proton transfer barrier was increased by investigating the PBI-NH$_3$ complex and the energy barrier was measured to be >868 cm^{-1}. In the complex, the solvent molecule was bound preferentially to the acidic (PBI)N-H group, resulting in a weaker hydrogen bonding between ammonia and the pyridyl-N atom and increase in the proton-transfer barrier width. The thorough experimental investigations aided by computational analysis provide a conclusive evidence of a novel deactivation pathway in the N-rich molecules.

References:

1. B. Barc, M. Ryszka, J.-C. Poully, E. J. Al Maalouf, Z. El Otell, J. Tabet, R. Parajuli, P. J. M. van der Burgt, P. Limão-Vieira and P. Cahillane, *Int. J. Mass Spectrom.* 365 (2014) 194-199.

2. H. Kang, K. T. Lee and S. K. Kim, *Chem. Phys. Lett.* 359 (2002) 213-219.

3. S. Saha and H. M. Quiney, *RSC Adv.* 7 (2017) 33426-33440.

4. A. Yoshikawa and S. Matsika, *Chem. Phys.* 347 (2008) 393-404.

5. S. Matsika, *J. Phys. Chem. A* 108 (2004) 7584-7590.

6. S. Perun, A. L. Sobolewski and W. Domcke, *J. Phys. Chem. A* 110 (2006) 13238-13244.

7. D. R. Weinberg, C. J. Gagliardi, J. F. Hull, C. F. Murphy, C. A. Kent, B. C. Westlake, A. Paul, D. H. Ess, D. G. McCafferty and T. J. Meyer, *Chem. Rev.* 112 (2012) 4016-4093.

8. J.-Y. Shen, W.-C. Chao, C. Liu, H.-A. Pan, H.-C. Yang, C.-L. Chen, Y.-K. Lan, L.-J. Lin, J.-S. Wang and J.-F. Lu, *Nat. Commun.* 4 (2013) 2611.

9. E. Nir, C. Plützer, K. Kleinermanns and M. De Vries, *Eur. Phys. J. D* 20 (2002) 317-329.

10. W. J. Schreier, P. Gilch and W. Zinth, Annu. Rev. Phys. Chem. 66 (2015) 497-519.

11. Y. Zhang, K. De La Harpe, A. A. Beckstead, L. MartínezFernández, R. Improta and B. Kohler, J. Phys. Chem. Lett. 7 (2016) 950-954.

12. X. Wang, Y. Yu, Z. Zhou, Y. Liu, Y. Yang, J. Xu and J. Chen, J. Phys. Chem. B 123 (2019) 5782-5790.

13. X. Wang, Z. Zhou, Y. Tang, J. Chen, D. Zhong and J. Xu, J. Phys. Chem. B 122 (2018) 7027-7037.

14. C. Jouvet, M. Miyazaki and M. Fujii, Chem. Sci. 12 (2021) 3836-3856.

15. E. Nir, C. Janzen, P. Imhof, K. Kleinermanns and M. S. de Vries, *J. Chem. Phys.* 115 (2001) 4604-4611.

16. C. Plützer, I. Hünig, K. Kleinermanns, E. Nir and M. S. De Vries, *ChemPhysChem* 4 (2003) 838-842.

17. E. Nir, L. Grace, B. Brauer and M. S. De Vries, *J. Am. Chem. Soc.* 121 (1999) 4896-4897.

18. R. Knochenmuss, O. Cheshnovsky and S. Leutwyler, Chem. Phys. Lett. 144 (1988) 317-323.

19. E. Samoylova, V. R. Smith, H. H. Ritze, W. Radloff, M. Kabelac and T. Schultz, J. Am. Chem. Soc. 128 (2006) 15652-15656.

20. C. Tanner, C. Manca and S. Leutwyler, Science 302 (2003) 1736-1739.

21. W. Domcke and A. L. Sobolewski, Science 302 (2003) 1693-1694.

22. A. Douhal, S. K. Kim and A. H. Zewail, Nature, 378 (1995) 260-263.

23. M. Novo, M. Mosquera and F. Rodriguez, J. Phys. Chem. 99 (1995) 14726-14732.

24. T. N. Burai, T. K. Mukherjee, P. Lahiri, D. Panda and A. Datta, J. Chem. Phys. 131 (2009) 034504.

25. M. Guin, S. Maity and G. N. Patwari, J. Phys. Chem. A 114 (2010) 8323-8330.

26. S. R. Brishty, Md. J. Hossain, M. U. Khandaker, M. R. I. Faruque, H. Osman and S. M. A. Rahman, Front. Pharmacol. 12 (2021) 762807.

27. F. Scott, A. M. Fala, L. E. Pennicott, T. D. Reuillon, K. B. Massirer, J. M. Elkins and S. E. Ward, Bioorg. Med. Chem. Lett. 30 (2020) 127040.

28. W. Domcke, J. Ehrmaier and A. L. Sobolewski, ChemPhotoChem 3 (2019) 10-23.

29. S. Maity, R. Knochenmuss, C. Holzer, G. Féraud, J. Frey, W. Klopper and S. Leutwyler, J. Chem. Phys.145 (2016) 164304.

30. S. G. Balasubramani et al. Chem. Phys. 152 (2020) 184107.

31. S. Khodia and S. Maity, Phys. Chem. Chem. Phys. 24 (2022) 12043-12051.

32. S. Khodia, R. Jarupula, S. Baweja, M. Shabeeb, B. Kalal and S. Maity, Phys. Chem. Chem. Phys. 25 (2023) 13498-13507.

33. R. Jarupula, S. Khodia, M. Shabeeb and S. Maity, Phys. Chem.Chem. Phys.25 (2023) 17010-17020.

34. P.J. Linstrom, W.G. Mallard, (Eds.), NIST Chemistry WebBook, NIST StandardReference Database Number 69, National Institute of Standards andTechnology, Gaithersburg MD, 20899.

Dr. Surajit Maity *completed his PhD from IIT Bombay in 2011. He joined as post-doctoral researcher at the Department of Chemistry and W. M. Keck research laboratory at the University of Hawaii at Manoa , followed by post-doctoral research works at University of Basel and Bern, Switzerland. He joined IIT Hyderabad in 2016 as an assistant professor. He is currently working as an associate professor. His research interest includes laser spectroscopy of molecules and clusters, development of novel laser spectroscopic techniques to determined energetics of reactions, photo stability of bioorganic chromophores.*

Simran Baweja *joined Ph.D. in 2019 with Dr. Surajit Maity at the Department of Chemistry, Indian Institute of Technology Hyderabad. She received her Ph.D. degree recently in 2024. Her doctoral research interests focused on the understanding of structures, bonding and energetics of biomolecular analogues in the gas phase employing various state-of-art laser spectroscopic techniques aided by quantum chemical calculations.*

Pulse Duration-Dependent Dissociation Dynamics of CH$_3$I

Arnab Sen[1], R. Gopal[2] and Vandana Sharma[3*]
[1]Indian Institute of Science Education and Research, Pune 411008, India
[2]Tata Institute of Fundamental Research, Hyderabad 500046, India
[3]Indian Institute of Technology Hyderabad, Kandi 502285, India
(email: vsharma@phy.iith.ac.in)

Abstract

This study investigates the dissociation dynamics of CH$_3$I under ultrafast laser pulses ranging from 25 fs to 1500 fs at moderate intensities. Using velocity map imaging and quantum chemistry calculations, we explore the role of orbital rearrangements and nuclear dynamics in ionization and fragmentation. The results show significant pulse-duration dependence, with shorter pulses favoring low-energy fragmentation channels and longer pulses promoting Coulomb explosion (CE) and higher-energy fragments. Time-of-flight spectra and multi-hit coincidence maps reveal complex dissociation pathways, including the formation of tri-cations at longer pulse durations. Our findings highlight the importance of pulse duration in influencing fragmentation channels and intermediate states during multi-orbital ionization.

Introduction

Intense laser-molecule interactions reveal complex dynamics from coupled electronic and nuclear motions, including bond softening, hardening, and enhanced ionization, well-studied in simple molecules like H$_2^+$ and D$_2^+$(1-6). Extending this to multi-electronic molecules (e.g., O$_2$, N$_2$, CO$_2$, CH$_3$I)(7-11) adds complexity due to multiple orbitals and electronic states, influenced by nuclear motion and orbital symmetries. Time-resolved experiments require sub-10 fs pulses for diatomics, but molecules like CH$_3$I, with slower vibrational motion, allow studies with 25 fs pulses. Geometry of CH$_3$I and spin-orbit coupling lead to rich dissociation dynamics. This work investigates CH$_3$I dissociation under 25 fs to 1.5 ps laser pulses, using velocity map imaging and quantum chemistry to explore orbital rearrangements and nuclear dynamics in the process.

Experimental Setup

The Femtopower V system (Spectra-Physics, Austria) generates few-mJ laser pulses at 1 kHz and 800 nm, with a ~25 fs pulse duration measured after the amplifier unit. Pulse durations can be varied by adjusting the compressor grating separation, with durations up to 75 fs determined by grating dispersion. The laser's linear polarization can be aligned using a $\lambda/2$ plate, and the beam is focused to a ~70 μm spot with a 30 cm focal length lens, achieving an intensity of ~5×10^{12} W/cm^2.

The ion-imaging spectrometer (12)is used to capture 3D velocity distributions of fragment ions. CH$_3$I vapor is introduced near the laser focus, and experiments are conducted in two modes: (a) imaging mode (polarization perpendicular to the spectrometer axis) for 3D distributions, and (b) time-of-flight (ToF) mode (polarization parallel to the spectrometer axis). Velocity distributions are recorded for 2 hours per pulse duration, ensuring consistent shot counts and gas pressure. Spectrometer voltages are optimized to capture full velocity images within the detector area.

ToF flight times enable calculation of ion kinetic energies, verified by the detector's multihit capability (up to 8 ions, <10 ns dead time). Photoion-photoion coincidences identify high-energy ions and determine their mean ion energies. The gas pressure is kept low (≤300 Hz ion count rate) to avoid false coincidences.

Measurements use positive second-order dispersion, with negligible differences observed when using negative dispersion.

Results:

Time-of-Flight Spectrum, Multi-Hit Coincidence and Correlation Map

Figures 1-left and right present the time-of-flight spectra of ionic fragments resulting from the interaction of methyl iodide with an 800 nm laser pulse at peak intensity 5×10^{12} W/cm^2 for two pulse durations: ~25 fs and ~1500 fs. In both cases, prominent peaks correspond to the parent ion CH_3I^+, singly charged methyl fragments (CH_n^+, n=0–3), and iodine ions (I^{q+}, q=0–2).

Significant differences emerge between the spectra for the two pulse durations. For the shortest pulse (~25 fs), CH_3^+ dominates the ionic fragments. In contrast, longer pulses (~1500 fs) yield a broader distribution of fragments, including higher-energy I^+ ions and the appearance of a new species, I^{2+}. These changes indicate an increased contribution from higher-energy fragmentation channels at longer pulse durations.

Identifying the parent molecular ions based solely on time-of-flight spectra is challenging. To resolve fragmentation pathways, a 2D histogram (Correlation Map) of ions detected in coincidence—showing the time-of-flight of first and second ions—provides critical insights.

Figures 2a and 2b illustrate photoion-photoion coincidence maps for pulse durations of ~25 fs and ~1500 fs, respectively. For the shorter pulse, a single set of coincidence islands corresponds to fragment pairs $CH_n^+ + I^+$, primarily arising from the concerted breakup of CH_3I^{2+}.

For the longer pulse (~1500 fs), two distinct sets of islands emerge, representing fragment pairs:

1. $CH_n^+ + I^+$
2. $CH_n^+ + I^{2+}$

Each set includes four pairs of islands, attributed to coincident detection of CH_3^+, CH_2^+, CH^+, and C^+ with either I^+ or I^{2+}. Some uncorrelated diagonal events are also observed, attributed to false counts. However, imposing suitable conditions allows for the isolation of true coincidence events.
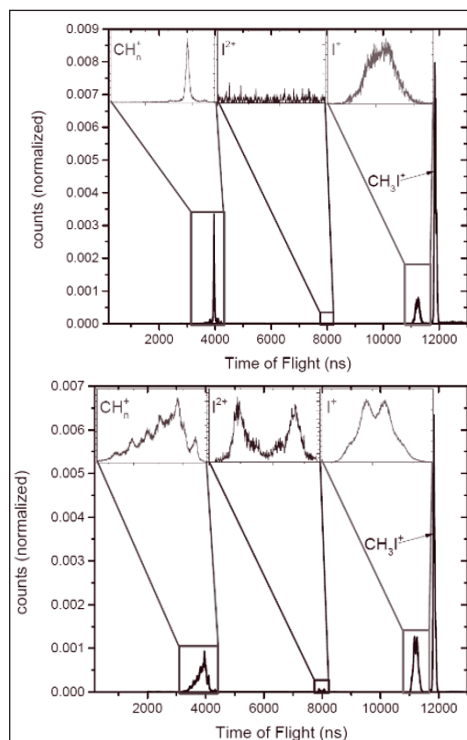

Fig1: Top) The time of flight spectrum at a pulse duration of ~25 fs with peak intensity 5×10^{12} W/cm^2 with the main fragments highlighted and their peaks shown in an expanded form. Bottom) at a pulse duration of ~1500 fs with peak intensity 5×10^{12} W/cm^2

The distinct nature of these islands suggests energetic, back-to-back, concerted fragmentation processes originating from CH_3I^{2+} and CH_3I^{3+}. These observations provide detailed insights into the underlying ionization and fragmentation dynamics.

Effects of Pulse Duration Variation

Spectra were recorded for pulse durations ranging from 25 fs to 1500 fs while maintaining a constant peak laser intensity. Figure 3 illustrates the variation in ion yields derived from the peak areas in the time-of-flight spectrum. The yield of

the parent molecular ion (CH_3I^+) remains largely unchanged with pulse duration. In contrast, the yields of high-energy fragments, particularly in the $CH_n^+ + I^+$ islands, show a steady increase up to ~1000 fs before reaching saturation.
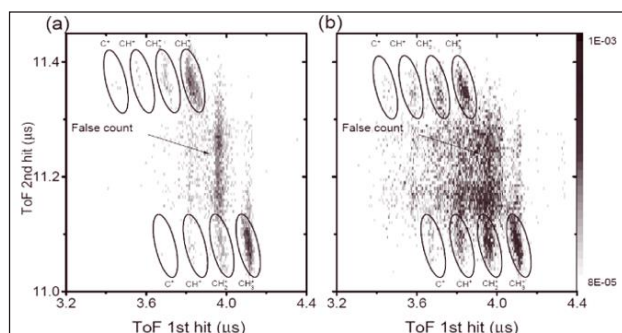

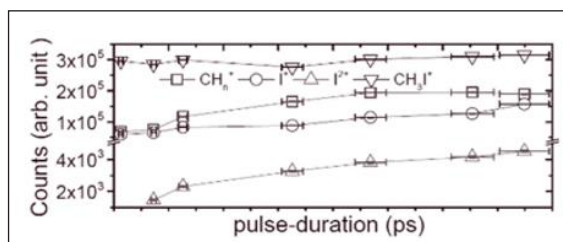*Fig2: Coincidence plot of the ions and ions for (a) ~ 25fs and (b) ~ 1500fs*

Fig 3: The measured absolute yields of the parent molecular ion CH_3I^+, the, and ions, derived from the area under the corresponding peaks.

Identification of Fragmentation Pathways

To understand the electronic states involved in the dissociation processes, the complete kinetic energy (KE) distribution and angular distribution of the ionic fragments were analysed. Time-sliced velocity map images of the major ionic fragments were recorded at various pulse durations, maintaining constant peak intensity.

Figures 4a and 4b show the ion distribution maps for the central velocity slice (ions ejected in the plane parallel to the detector and laser polarization axis) of the CH_3^+ and I^+ fragments at the shortest pulse duration (~25 fs). The maps reveal two distinct regions: an isotropic outer ring for high-energy fragments and dense distributions near the centre for low-energy fragments. The KE distribution of these fragments, derived by integrating the counts over the azimuthal angle at each radius. The KE distribution, obtained through ToF spectrum analysis of energetic fragments, shows a close correspondence with the velocity map images, allowing identification of the outermost ring as a result of Coulomb explosion (CE) from doubly charged parent ions (13).

The low-energy fragments arise from the dissociation of singly charged molecular ions into ionic and neutral fragments. These fragmentation channels can be labelled using a (p;q) notation, where p and q represent the charge states of CH_p^+ and I_q^+ ions, respectively. The KE distributions for CH_3^+ and I^+ ions at ~25 fs were fitted to
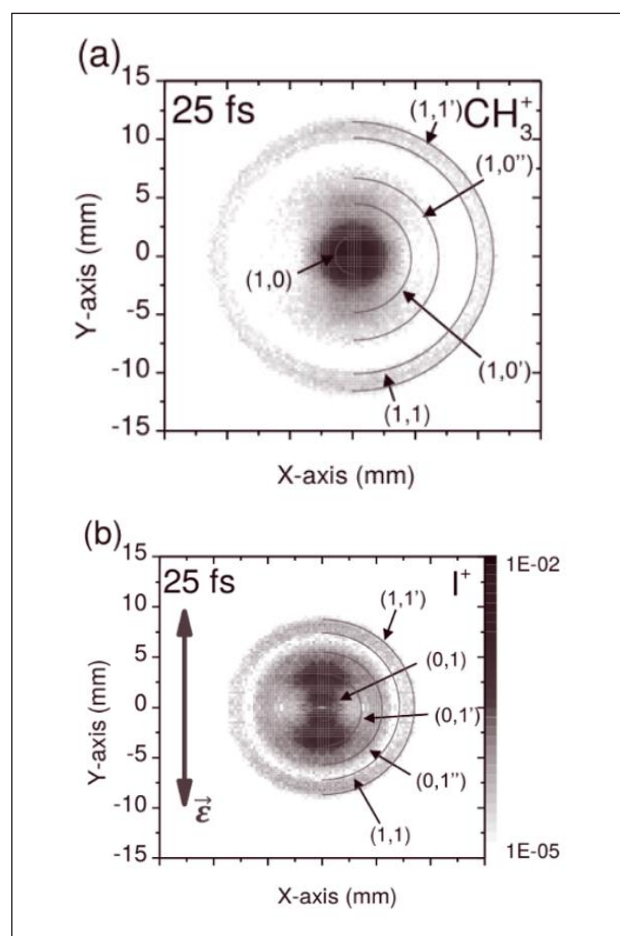

Fig4: Velocity Map Images of (a) and (b) I^+ ions at the shortest pulse duration. The color scale for ion counts is logarithmic. The laser polarization axis (red arrow) is vertical. Semicircles identify different dissociation and CE channels.

Gaussian distributions, with three peaks for low-energy fragments and two for CE fragments. While the CE peaks are evident for CH_3^+ fragments, they are less distinguishable for I^+ due to lower energy resolution (13). For more details see 13. At higher intensities, the CE channels are more populated, but no new channels emerge, and the CE peak positions remain unchanged.

For the pulse durations used here, CH_3I^+ predominantly populates the spin-orbit split ground states and , dissociating into CH_3^+ and neutral I atoms. The excited state contributes to the formation of near-zero energy I^+ ions in fast non-adiabatic ionization. Higher excited states may also participate in dissociation through multi-photon coupling. Arnab et al (see table 1 in 13) lists possible dissociation pathways, although low-energy channels are not uniquely assigned.

The CE channels at ~2.9 eV and ~3.5 eV are attributed to repulsive electronic states of the doubly charged parent ion, leading to CH_3^+ + I^+ fragments, where I^+ in the $^3P_{1,0}$ and $^3P_2$ states.

I^{2+} ions, arising from the dissociation of dications or the CE of trications, were also detected in the imaging mode. At a pulse duration of ~25 fs, no I^{2+} ions were observed, suggesting that tri-cation formation is not feasible at these intensities. However, for a pulse duration of ~150 fs, I^{2+} ions were detected, with the KE distribution fitted to three Gaussian distributions. The peak at ~0.2 eV is attributed to the dissociation of CH_3 I^{2+} ions via the (0;2,0) channel, while the high-energy peak at ~0.8 eV corresponds to a Coulomb explosion channel (1;2). This assignment aligns with previous studies, although differences in KE distributionsmay arise due to variations in pulse duration and intensity.

The formation of I^{2+} highlights the strong pulse duration dependence of the dissociation process. At ~25 fs, tri-cation formation is unlikely, while at ~150 fs, the production of I^{2+} becomes significant, further emphasizing the role of pulse duration in determining fragmentation pathways.

Effects of Pulse Duration Variation

As pulse duration increases, the relative intensities of dissociation channels change, but no new channels or energy shifts are observed (Figure 5 shows ion velocity distributions for CH_3^+ and I^+ at pulse durations of 25 fs, 150 fs, 650 fs, and 1500 fs with constant laser intensity). The Coulomb explosion (CE) channels (1;1) and (1;1') merge and shift to lower energies, with the Kinetic Energy Release (KER) reducing from 3.6 eV and 4.1 eV at 25 fs to a broad peak at 3.2 eV at 1500 fs (see 13 for more details). Additionally, as can be seen in fig 5 the distribution becomes increasingly anisotropic with longer pulse durations, and the relative yield of the CE channels increases, as observed in ToFmode.

In ToF mode, the yields of dehydrogenated methyl fragments (CH_m^+, m = 0–2) also enhance with pulse duration. The kinetic energy distributions of these fragments at 1500 fs show
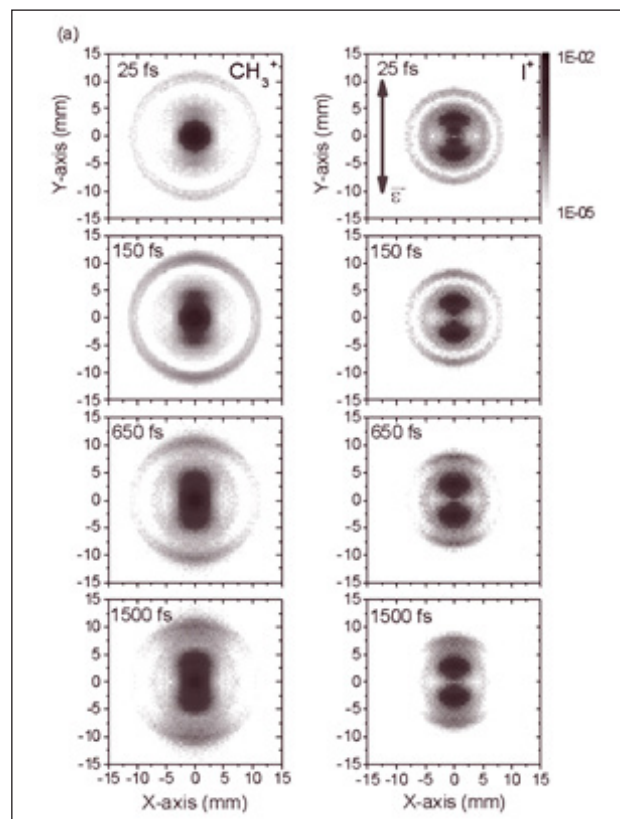

Fig 5: Time sliced velocity map images of [left panel] and [right panel] I^+ ions recorded at different laser pulse durations.

the following mean KE values: CH_3^+ (2.9 eV), CH_2^+ (2.8 eV), CH^+ (2.7 eV), and C^+ (2.6 eV). The trend in kinetic energy ordering (remains unchanged with varying pulse durations. The spectrometer's resolution in ToF mode is 0.08 eV, and the mean kinetic energy differences between these dehydrogenated fragments are independent of pulse duration, suggesting a stepwise dissociation mechanism.

The stepwise dissociation pathway for CH_3^+ after the Coulomb explosion of the parent ion follows:

- $CH_3^+ \rightarrow CH_2^+ + H$
- $CH_2^+ \rightarrow CH^+ + H$
- $CH^+ \rightarrow C^+ + H$

In each step, the neutral H atom carries away a small amount of energy, leading to a shift in the kinetic energy of the dehydrogenated fragments.

No I^{2+} ions were observed at 25 fs, indicating that tri-cation generation is not feasible at these intensities. The angular distribution of the CE channel (1;2) does not change significantly with increasing pulse duration, but the yield increases and the CE peak shifts to lower energy (0.6 eV at 1500 fs).

Time Evolution of Intermediate States

When CH_3I interacts with an ultrashort laser pulse of 25 fs duration in the moderate intensity range (10^{12}–10^{13} W/cm²), ionization primarily occurs in the spin-orbit coupled CH_3I^+ states, where a single electron is removed from the outermost orbital (2e). This process is a rapid, non-adiabatic transition akin to the Frank-Condon effect. The low-energy dissociation channels observed at this short pulse duration suggest that lower-lying excited states, such as $\tilde{A}(2E_{1/2})$ and $\tilde{B}(3E_{3/2}\ and\ 5E_{1/2})$, and , are also populated through direct ionization. This ionization excites multiple ro-vibrational levels, leading to the formation of a wavepacket that evolves along the potential energy surface defined by the C-I bond length.

For the di-cation states, direct ionization is dominant at equilibrium geometry for short pulses, but for longer pulses, sequential ionization from the intermediate mono-cationic states becomes more significant. As a result, the yield of subsequent Coulomb explosions (CE) is influenced by the evolving dynamics of these intermediate states.

Photon-Induced Orbital Coupling

We propose that the variations in the yield and angular distributions observed in the CE channels are a result of these evolving dynamics. To investigate this, we performed multi-configuration self-consistent field (MC-SCF) calculations using the GAMESS quantum chemistry package under field-free conditions. These calculations examined the variation in the orbital energy of the outer orbitals as the C-I bond length changes, with the geometry of the CH_3 group held constant. Using N-21G split valence basis set and NGAUSS=3, the results (Figure 5) show that the energy of the inner HOMO-1 (3a) orbital increases with bond elongation. The HOMO (2e) and HOMO-1 (3a) orbitals merge around ~ 4.5 Å (see fig 6), but at a C-I bond length of ~ 3.9 Å, the energy difference
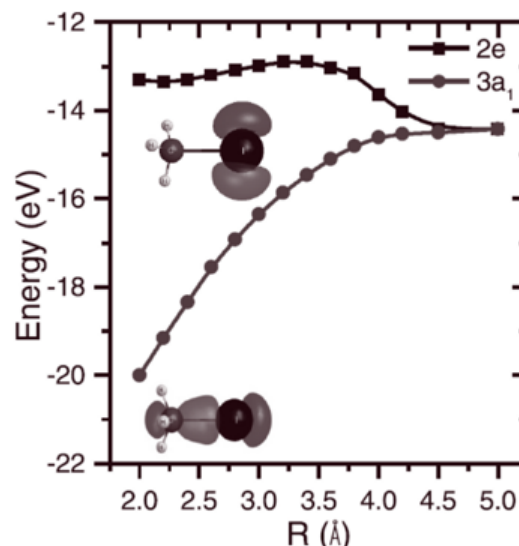

Fig6: The energy of the HOMO 2e and HOMO-1 $3a_1$ orbitals of the monocationic Methyl Iodide obtained from MCSCF calculation. The orbital structres of 2e and $3a_1$ orbitals are shown in the inset.

between them matches the photon energy of ~ 1.5 eV, suggesting efficient orbital coupling in the presence of the laser field. This orbital coupling likely drives the observed variations in yield and angular distributions in the CE channels.

Discussion:

Multi-orbital ionization constrains the angular distribution of fragment ions. At the shortest pulse duration (25 fs), the Coulomb explosion (CE) channels exhibit a nearly isotropic distribution, consistent with ionization from the outermost HOMO (2e) orbital. As the pulse duration increases beyond 650 fs, the CE channels broaden and shift to lower energy, with the angular distribution becoming more anisotropic, indicating greater involvement of the HOMO-1 (3a) orbital. This orbital, aligned along the C-I bond, becomes easier to ionize when the laser polarization axis is parallel to the bond, leading to the observed anisotropy in the CE distribution. At longer pulse durations, ionization from the state dominates, with increasing involvement of the 3a orbital at larger inter-nuclear separations.

The (1,2) CE channel originates from ionization of the tri-cationic state of CH_3I. Direct ionization to the tri-cation is unlikely at moderate intensities, so sequential ionization, facilitated by C-I bond stretching, is more probable. We suggest that the upward shift in orbital energy in the intermediate Ae state increases ionization probability, leading to tri-cation formation. For pulses around 150 fs, I^{2+} ions show a broad energy distribution peaked at ~0.82 eV, with a strongly anisotropic angular distribution, indicating a dominant contribution from the HOMO-1 (3a) orbital.

Methyl ionic fragments also show increased anisotropy with pulse duration, reflecting greater involvement of the 3a orbital, which is aligned with the laser polarization axis. The C-I bond undergoes distortion due to the external electric field, initiating step-wise dissociation and sequential fragmentation. The correspondence of C^+ yields with model calculations supports this

hypothesis. The role of intermediate electronic states and quantum calculations involving transient species with varying geometries warrants further investigation.

The laser pulse chirp does not affect fragmentation product yields or energies, unlike in previous studies where chirp influenced the yields and energies. Our data, showing no significant shift in dissociation energies, suggest that chirp does not play a critical role here. More details can be found in (13).

Although the classical model estimates the critical inter-nuclear distance for ionization, the discrepancies at shorter pulse durations may arise from neglecting direct ionization effects and errors in the potential energy curve due to fixed geometry assumptions. Future time-domain Schrödinger equation solutions are needed to confirm the observed kinetic energy release (KER) and refine the ionization pathway.

Summary:

When CH_3I interacts with moderate-intensity laser pulses (5×10^{12} W/cm², 25 fs–1500 fs), it is primarily singly ionized, with many of these ions dissociating further in the laser field. Despite low energy densities, longer pulse durations (>150 fs) can lead to the formation of di-cationic and tri-cationic states. Our ion imaging and a classical 1-D model suggest that delayed sequential ionization in the intermediate Ae state of the mono-cation plays a key role. As the C-I bond stretches, the energy of the inner 3a orbital increases. If the laser intensity is sufficient, resonant coupling can occur, enhancing electron transfer (3a → 2e). This allows longer pulses to further populate repulsive states of CH_3I^{2+} and CH_3I^{3+} ions. CH_3I remains a highly dynamic system, and further experimental and theoretical studies are needed to explore these processes in detail.

References:

1. P. H. Bucksbaum, A. Zavriyev, H. G. Muller, and D. W. Schumacher, Phys. Rev. Lett.,64, 16, 1883– 1886,(1990).
2. L. J. Frasinski, J. H. Posthumus, J. Plumridge, K. Codling,

P.F. Taday, and A. J. Langley, Phys. Rev. Lett., 83, 18, 3625–3628 (1999).

3. D. Pavicic, A. Kiess, T. W. Hänsch, and H. Figger, Phys. Rev. Lett., 94, 16, 163002 (2005).

4. T. Zuo and A. D. Bandrauk, Phys. Rev. A, 52, 4, R2511–R2514 (1995).

5. A. D. Bandrauk, and J. Ruel, Phys. Rev. A, 59, 3, 2153–2162(1999).

6. S. Erattupuzha, C.L. Covington, A. Russakoff, E. Lötstedt, S. Larimian, V. Hanus, S. Bubin, M. Koch, S. Gräfe, A. Baltuska, X. Xie, K. Yamanouchi, K. Varga and M. Kitzler, J. Phys. B: At. Mol. Opt. Phys., 50, 12, 125601 (2017).

7. L. J. Frasinski, J. Plumridge, J. H. Posthumus, K. Codling, P. F. Taday, E. J. Divall and A. J. Langley, Phys. Rev. Lett., 86, 2541, (2001).

8. M. E. Corrales, G. Gitzinger, J. González-Vázquez, V. Loriot, R. de Nalda, and L. Bañares,J. Chem. Phys., 116, 2669, (2012).

9. D. Zhang, S. Luo, H. Xu M. Jin, F. Liu, B. Yan, Z. Wang, H. Liu, D. Jiang, A. Eppink, W. Roeterdink, S. Stolte, and D. Ding,Eur. Phys. J. D 71, 148, (2017).

10. H. Liu, Z. Yang, Z. Gao, and Z. Tang, J. Chem. Phys., 126, 044316, (2007).

11. Y. Wang, S. Zhang, Z. Wei, and B. Zhang, J. Phys. Chem. A, 112, 3846, (2008)

12. R. Gopal, A. Sen, S. R. Sahu, A. S.Venkatachalam, M. Anand, and V. Sharma, Rev. Sci. Instrum. 89, 086107 (2018).

13. Arnab Sen, S. Mandal, S. Sen, B. Bapat, R. Gopal, and V. Sharma Physical Review A, Vol. 103, 4, 043107 (2021)

	Dr. Arnab Sen did his PhD from IISER, Pune. His research involves real-time imaging of coupled electronic and nuclear wavepacket dynamics in photo-excited molecules to unravel ultrafast chemical processes using advanced pump-probe spectroscopy. During his PhD, he gained expertise in Photo-ion and Photo-electron Spectroscopy and contributed to setting up a Velocity Map Imaging spectrometer and a Reaction Microscope. Currently, as a postdoctoral researcher, Dr. Sen employs Time-Resolved X-ray Absorption Spectroscopy to explore ultrafast reactions at the Carbon and Nitrogen K-edges, advancing our understanding of molecular transformations.
	Dr. Ram Gopal, a physicist with a PhD from the Max-Planck Institute for Nuclear Physics in Heidelberg, Germany, serves as a Scientific Officer at the Tata Institute of Fundamental Research in Hyderabad. Leveraging his expertise, he designs, develops, and maintains cutting-edge instrumentation, advancing our understanding of intense laser-matter and plasma interactions. His research focuses on elucidating the dynamics of atoms and molecules interacting with intense, ultrashort laser beams featuring tailored structural properties.
	Dr. Vandana Sharma, Professor of Physics at IIT Hyderabad, is a renowned expert in ultrafast lasers, atomic and molecular physics, and biomedical optics. Her research spans over two decades, focusing on EUV photon sources, charged particle imaging, and healthcare technologies like 3D Vein Viewers. She completed her PhD at PRL, Ahmedabad, and pursued postdoctoral research at institutions like Max-Planck Institute and JILA. With numerous high-impact publications and awards, including the Sheldon Datz Best Scientist Award, Dr. Sharma is dedicated to advancing science and developing innovative, accessible solutions for societal benefit.

INDIAN SOCIETY FOR RADIATION AND PHOTOCHEMICAL SCIENCES

(Reg. No. 617/1985, GBBSD, Bombay; Trust No. F-10965)

Radiation & Photochemistry Division

Bhabha Atomic Research Centre, Mumbai - 400 085

Member Enrolment Form

1. Name in Block Letters:

2. Date of Birth:

3. Highest Academic Qualification:

4. Present Position:

   Photograph

5. Addresses:

Office	Residence
Telephone	Telephone
E-mail	E-mail

6. Address for Correspondence: Office / Residence

7. Category of Membership Applied for: Annual / Life /Corporate member

Category	Fees	Admission fee	Total Amount
Annual	Rs 200/-	Rs 100/-	Rs 300/-
Life Member	Rs 2000/-	Rs 100/-	Rs 2100/-
Corporate Member	Rs 20000/-	Rs 1000/-	Rs 21000/-

8. ***Remittance:** DD in favour of 'ISRAPS' payable at MUMBAI
   For Bank Transfer:
   A/c No.10536133801, SBI, BARC Branch, IFSC SBIN0001268
   (e-mail the money transfer details along with the details requested above
   to: **israps.secretary@gmail.com** and copy to **mathip@barc.gov.in)**
   *Payment can be made after the approval of application by Secretary, ISRAPS

9. Brief Resume of activities and research interests:
   (min. 500 words, in a separate attachment)

10. List of memberships of other professional bodies, if any:

11. List of prizes/awards/fellowships received, if any:

12. Number of Publications
    (Pl. attach complete list)

 I agree to abide by the constitution and bye-laws, and rules and regulations of the SOCIETY.

Place:

                                                    Signature

Date:

Contents